Integrated Modeling of Optical Performance for the Terrestrial Planet Finder Structurally Connected Interferometer

by

David M. LoBosco
S.B. Aeronautical and Astronautical Engineering
Massachusetts Institute of Technology, 2002

Submitted to the Department of Aeronautics and Astronautics
in partial fulfillment of the requirements for the degree of

Master of Science

at the

MASSACHUSETTS INSTITUTE OF TECHNOLOGY

June 2004

Author .....
Department of Aeronautics and Astronautics
May 21, 2004

Certified by.....
David W. Miller
Associate Professor of Aeronautics and Astronautics
Thesis Supervisor

Accepted by .....
Edward M. Greitzer
H.N. Slater Professor of Aeronautics and Astronautics
Chairman, Department Committee on Graduate Students

Integrated Modeling of Optical Performance for the Terrestrial Planet Finder Structurally Connected Interferometer

by

David M. LoBosco

S.B. Aeronautical and Astronautical Engineering

Massachusetts Institute of Technology, 2002

Submitted to the Department of Aeronautics and Astronautics
on May 21, 2004, in partial fulfillment of the
requirements for the degree of
Master of Science

Abstract

The Terrestrial Planet Finder (TPF) mission, to be launched in 2014 as a part of NASA's Origins Program, will search for Earth-like planets orbiting other stars. One main concept under study is a structurally connected interferometer. Integrated modeling of all aspects of the flight system is necessary to ensure that the stringent dynamic stability requirements imposed by the mission are met.

The MIT Space Systems Laboratory has developed a suite of analysis tools known as DOCS (Disturbances Optics Controls Structures) that provides a MATLAB environment for managing integrated models and performing analysis and design optimization. DOCS provides a framework for identifying critical subsystem design parameters and efficiently computing system performance as a function of subsystem design. Additionally, the gradients of the performance outputs with respect to design variables can be analytically computed and used for automated exploration and optimization of the design space.

The TPF integrated model consists of a structural finite element model, optical performance model, reaction wheel isolation stage, and attitude/optical control systems. The integrated model is expandable and upgradeable due to the modularity of the state-space subsystem models. Optical performance under reaction wheel disturbances is computed, and the effects of changing design parameters are explored. The results identify redesign options that meet performance requirements with improved margins, reduced cost and minimized risk.

Thesis Supervisor: David W. Miller
Title: Associate Professor of Aeronautics and Astronautics

Acknowledgments

This research was performed for the Jet Propulsion Laboratory under JPL Contract #1250253 (TPF Interferometer Trades and Model Development) with Technical/Scientific Officers Dr. Curt Henry and Dr. Brent Ware, and JPL Contract #1255406 (Model Verification) with Technical/Scientific Officer Dr. Marie Levine-West. Ms. SharonLeah Brown served as MIT Fiscal Officer for both contracts.

Contents

List of Figures

List of Tables

Chapter 1

Introduction

NASA's Origins Program seeks the answers to fundamental questions of life in the universe such as "Where did we come from?" and "Are we alone?" The flagship of the Origins Program is the Terrestrial Planet Finder (TPF). TPF will be launched in 2014 and will search for Earth-like planets orbiting other stars. A mission like TPF is only now becoming a possibility because of recent advancements in planet detection techniques and demonstrated success by high-precision space-based optical observatories. Even so, much technology still needs to be developed for this spacecraft. Scientists and engineers are still involved in early trade studies to determine which architecture will best serve the needs of TPF.

This first chapter is meant to provide background information about the TPF mission and explain the motivation for the research presented in this thesis. An overview of the thesis is also provided.

1.1 Planet Finding

Already, over 110 extrasolar planets have been discovered using three indirect detection techniques. These techniques rely on observing the effect the planet has on its parent star rather than observing the actual planet. Only very massive planets, on the order of Jupiter's mass, have enough effect on the star to be detected by these methods. In order to find Earth-like planets, new techniques must be developed.

1.1.1 Current Planet Detection Methods

The first technique of detecting extrasolar planets is known as the "radial velocity" method. This technique relies on the Doppler effect where light waves from a star moving towards the observer will tend to shift towards the blue end of the spectrum and light waves from a star moving away from the observer will tend to shift towards the red end of the spectrum. By observing a periodic change between blue shift and red shift, the presence of a planet can be deduced.

The second technique, "astrometry," measures the change in a nearby star's location relative to very distant stars that appear to be fixed. Periodic motion in the star will be caused by the gravitational interaction of an orbiting planet.

The third technique is the "planetary transit" method. This technique requires that a planet's orbital inclination be aligned with the line of sight between the observer and the parent star. The observer must also be looking at the star during the small fraction of the orbital period where the planet passes in front of the star disc. A periodic reduction in the number of photons received from a star will imply the periodic transit of a planet as it orbits the star [11].

1.1.2 Terrestrial Planet Finding

While current methods allow for the discovery of Jupiter-size extrasolar planets, new direct optical detection techniques are required to find terrestrial (Earth-like) planets. Terrestrial planets are not massive enough to have strong gravitational effects on the parent star and cannot be found through the indirect detection techniques. To accomplish direct optical detection, extremely high resolution telescopes are necessary. In addition, these telescopes must have a method of blocking out the light of the parent star to reveal the close orbiting planet.

Two candidate methods for blocking starlight and revealing orbiting planets are coronagraphy and nulling interferometry. A coronagraph uses a physical obscuration to block the light of the star and reveal the surrounding corona. Nulling interferometry uses destructive and constructive interference of multiple separated telescopes to both

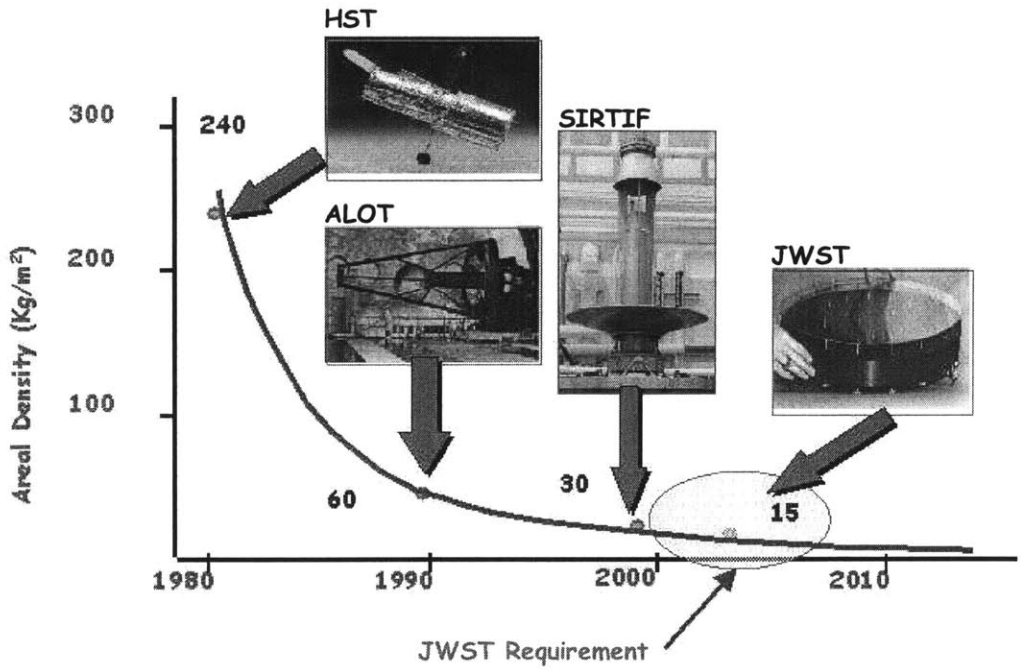

Figure 1-1: Reduction in area density of space-based optical systems over time [19].

block the star light and amplify the reflected light from the planet.

With direct optical detection of planet reflected light, spectral analysis can be used to determine the composition of the planet's atmosphere. Scientists will search for planets with the proper ratios of key elements such as oxygen and carbon dioxide that may indicate the existence of life. Furthermore, planet temperature and the presence of water can be determined using spectroscopy.

1.2 TPF Precursor Missions

A series of precursor missions are in the works to both validate technology and perform preliminary observations and measurements for TPF. A large planetary census will be taken through the use of ground-based interferometers (Keck, Large Binocular Telescope (LBT) and Very Large Telescope Interferometer (VLTI)) and the Space Interferometry Mission (SIM). In particular, SIM will use astrometry to measure the

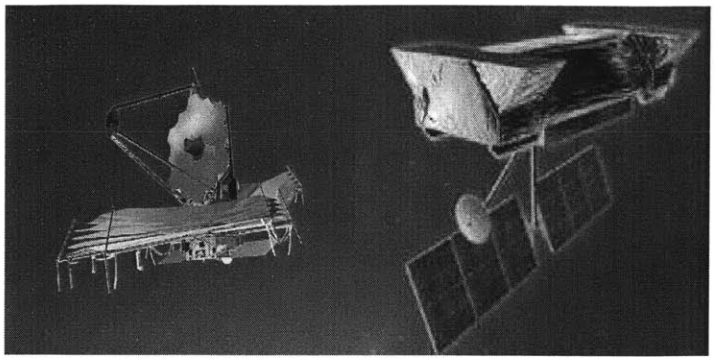

Figure 1-2: Artist renderings of JWST [19] (left) and SIM [17] (right).

precise location of stars and identify candidate planetary systems for TPF to explore further. These programs will also validate interferometry hardware and software and demonstrate nulling operations [11].

Furthermore, TPF will require the use of very large optical systems. The need for lightweight optics has been identified as a key technology driver for the success of large space-based optical systems. Figure 1-1 shows the progress in demonstrated lightweight optics. The James Webb Space Telescope (JWST), formerly known as the Next Generation Space Telescope (NGST), will demonstrate the use of optical elements with an areal density of 15 kg/m^2 [19]. This areal density requirement will be similar for TPF. JWST will also demonstrate cryogenic actuators and active coolers that will likely be used for TPF [11]. JWST and SIM are pictured in Figure 1-2.

1.3 TPF Design Overview

The two architectures currently under consideration for the Terrestrial Planet Finder Mission are a coronagraph and a large baseline interferometer. The coronagraph will consist of one large 8-10 m diameter telescope operating at room temperature and collecting light in the visible spectrum. It will have a billion to one image contrast and therefore require very precise optical control [2].

The interferometer will consist of four, 3-4 m diameter telescopes structurally connected or formation flown along a 40 m or greater baseline. These interferometer

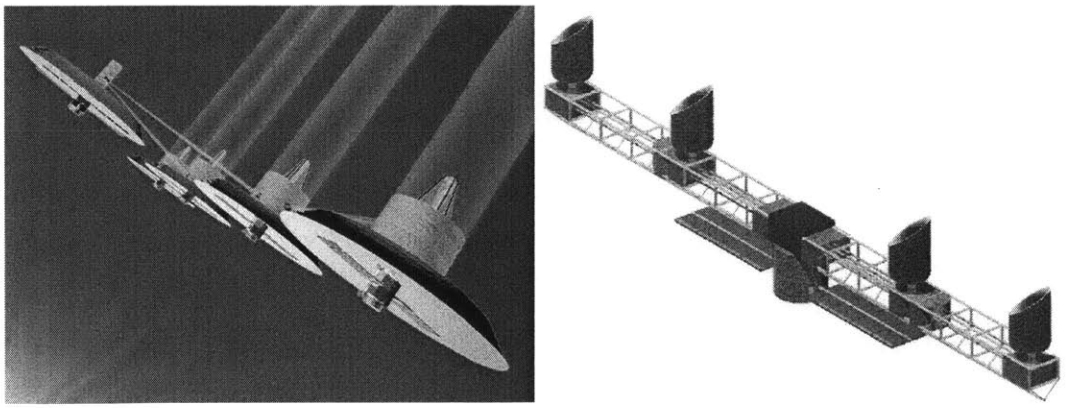

Figure 1-3: Possible mission architectures for TPF: Formation flown (left) and structurally connected (right) interferometers [22].

architectures are shown in Figure 1-3. The interferometer will operate at cryogenic temperatures of approximately 40 Kelvin and will collect light in the infrared spectrum. The image contrast will be a million to one and therefore the optical control requirements will be relatively less stringent than for the coronagraph [2].

1.3.1 Nulling Interferometry

In this thesis we will focus on the structurally connected interferometer (SCI) architecture. The nominal SCI design utilizes a rotating dual-Bracewell interferometer [11]. The main performance metrics for SCI are null depth and null stability. Null depth is the ratio of interferometer response at the star limb over interferometer response at the planet. This measurement basically tells us if enough of the starlight is blocked to be able to see the planet. Null stability places requirements on systematic noise and the number of stellar photons that can leak through before a false planetary response is inferred [4].

Figure 1-4 shows two graphs that demonstrate the effects of an interferometer. The graph on the left shows the point spread function (PSF) for a single aperture (dashed line) and a two aperture interferometer (solid line). The first valley moving out from the center of the PSF defines the angular resolution of the system. It can be

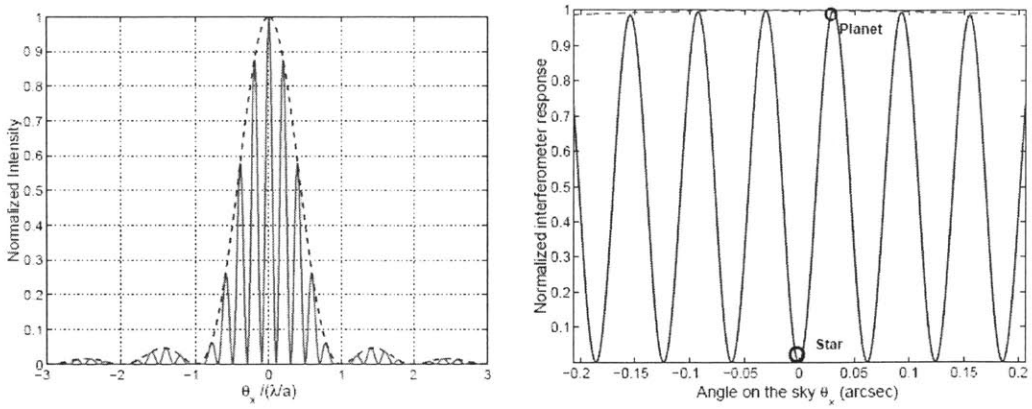

Figure 1-4: Normalized intensity of two rectangular apertures (left). Normalized nulling interferometer response for a family of apertures [22].

seen that the interferometer (solid line) has a much smaller angular resolution. This means that it can see more distinguishable characteristics of distant objects than the single aperture telescope can.

The graph on the right shows the normalized interferometer response for a nulling interferometer with many apertures. In this case, the central fringe is dark. Since the light beams from the apertures are combined out of phase, a valley is produced at the center where the star is located and a peak is produced at the location of the planet. This has the effect of blocking the light from the star and magnifying the light from the planet.

Figure 1-5 shows the interferometer response for a varying number of apertures. Null depth is calculated by dividing the interferometer response at the solar radius by the interferometer response at the planet. Since the plot is normalized so that the interferometer response at the planet is unity, the null depth is equal to the interferometer response at the solar radius. The analysis used to generate this plot set the null depth requirement at 10^{-6}. A minimum of three apertures would be needed to meet this requirement [22].

From the Null Depth and Null Stability requirements, a number of other requirements can be derived for contributing factors such as Optical Pathlength Difference (OPD), Differential Wavefront Tilt (DWT), and Differential Beam Shear (DBS).

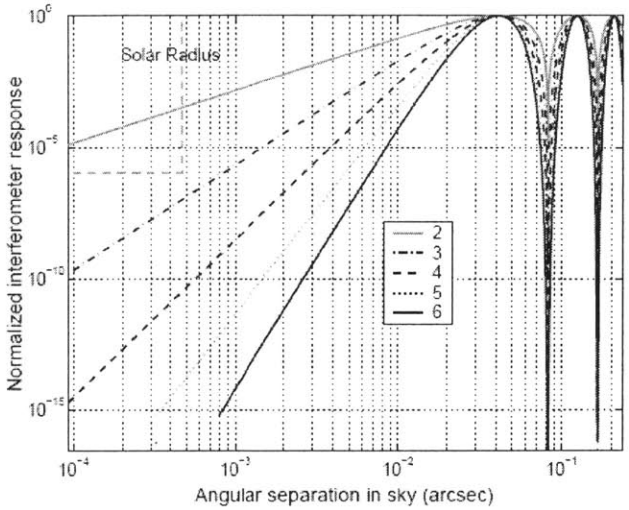

Figure 1-5: Normalized nulling interferometer response for varying number of apertures with null depth requirement [22].

These performance metrics must meet very stringent requirements under the influence of disturbances from sources such as reaction wheel imbalance and sensor noise.

1.4 Integrated Modeling

In order to validate that requirements can be met, as well as to determine redesign options, integrated modeling of the structural dynamics, controls, optics and disturbance sources of TPF is necessary. Integrated modeling of high precision optical systems has gained prominence in recent years. As such, a review of the relevant work in this area was performed before undertaking the challenge of modeling TPF.

Gutierrez developed an integrating modeling methodology for precision controlled structures [12]. In his work, he created separate models of the structure, controls, disturbances and performance and linked them together as state-space models. He applied this modeling method to SIM. Many of the methods developed by Gutierrez were applied to JWST (then NGST) by de Weck [8]. The work by de Weck and Gutierrez helped develop the DOCS (Dynamics-Optics-Controls-Structures) toolbox.

DOCS will be explained further in the next section.

Other efforts have been made to develop integrated modeling tools. Ball Aerospace has developed the "Integrated Telescope Model" (ITM) that utilizes the MATLAB®-Simulink® environment for performance modeling and analysis of space telescopes [21]. NASA's Jet Propulsion Laboratory developed the Integrated Modeling of Optical Systems (IMOS) toolbox for similar purposes. IMOS has been used extensively for the SIM modeling effort [10]. Integrated modeling is also being used for ground based systems such as the Thirty Meter Telescope (TMT) [9] and the Very Large Telescope Interferometer (VLTI) [27].

In this thesis, significant attention is given to the optical subsystem model and the automatic optical sensitivity matrix generation. Therefore, it is important to note previous work in this area that provides a foundation for our optical modeling efforts. Redding and Breckenridge derived equations for coordinate-free ray-trace analysis of large space-based optical systems [7]. A framework for linear optical sensitivity calculation was developed by Howard for JWST [15].

1.4.1 DOCS Framework

The DOCS (Disturbances-Optics-Controls-Structures) toolbox, created by the MIT Space Systems Laboratory and Midé Technology Corporation, provides a powerful framework for the modeling and analysis of precision opto-mechanical space systems. Utilizing the MATLAB environment, DOCS allows the user to create an integrated model of the spacecraft that simulates the structural dynamics, the controllers, and the optical layout. DOCS elements are created as state space objects and integrated models are generated by linking DOCS elements together. The integrated models are converted to the frequency domain to utilize stochastic broadband disturbance models. Disturbances are input into the system and root mean square optical performance metrics are calculated as the outputs.

Using the DOCS toolbox, we can analyze the integrated model in many ways. First, we can vary certain design parameters without re-running the entire model and determine the effect on performance. Doing this we can determine the sensitivity

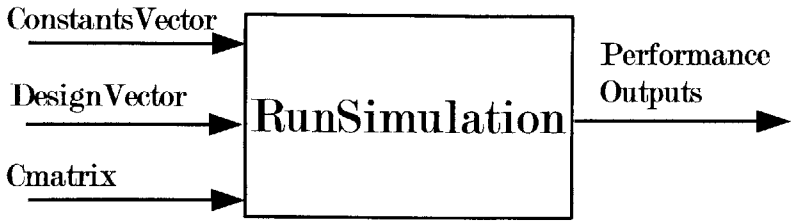

Figure 1-6: Diagram of RunSimulation inputs and outputs.

of performance to each design parameter and figure out which aspects of the design have the most effect on the overall performance. Moreover, we can produce modal variance contribution plots that allow for the identification of problematic vibration modes in the structure. Recommendations can be made to either redesign part of the structure or prevent disturbances in the problematic frequency ranges.

1.5 Motivation/Thesis Overview

The goal of this research is to create an integrated model of the TPF structurally connected interferometer that can predict optical performance and can be used in design trades to determine ways to improve optical performance. Given that TPF is still in its early development phase, it is expected that many parameters will change throughout the design process. Therefore, it is important that the integrated model is easily adaptable and evolvable as the design progresses and the requirements are better understood.

In order to meet the goal of adaptability, the entire integrated model generation and optical performance analysis is automated through the use of MATLAB. The user provides three inputs to the MATLAB function `RunSimulation`, and optical performance outputs are returned. As shown in Figure 1-6, the inputs are `DesignVector`, `ConstantsVector`, and `Cmatrix`. `DesignVector` and `ConstantsVector` contain the parameters that define geometry, material properties, control bandwidths, etc. for the different subsystem models. `DesignVector` contains those parameters which are expected to vary throughout the design process while `ConstantsVector` is made up of

the parameters expected to remain constant (at least in our analysis). The integrated model can "adapt" to changes in `DesignVector` and be automatically regenerated. `Cmatrix` is the optical sensitivity matrix that is calculated beforehand by another set of MATLAB functions. `Cmatrix` only needs to be recalculated for changes in the optical design and is therefore kept separate.

Design trades can also be performed by varying values in `DesignVector` and repeatedly regenerating the integrated model. Unfortunately, performing design trades by this method is very computationally intensive due to the costly finite element analysis. A better method is to designate certain parameters to be perturbable using DOCS during the integrated model generation. The sensitivities of performance with respect to these parameters are calculated so that the values can be altered after the integrated model is fully generated. Thus, performance is quickly recalculated without the need to regenerate and analyze the FEM.

We have explained that the integrated model of TPF can be adapted by changing values in `DesignVector`. But what happens if we want to add new subsystem models or improve the fidelity of an existing model? Since our TPF integrated model is created in state-space form, the subsystem models are very modular. Individual models can be drastically altered and still be used in the same integrated model as long as their inputs and outputs remain the same. Likewise, new models can be inserted between existing models provided that the inputs and outputs are consistent. If it is necessary, models can have additional inputs or outputs added as well.

It should now be understood that the integrated model of TPF is intended to be a continually evolving tool to aid in the design process. In this thesis, we will cover the current integrated model and explain why it is important to model specific subsystems at this time. We will also explain the justifications for the level of model fidelity and how the models have already evolved.

Figure 1-7 shows a block diagram of the integrated model of TPF. Some of the subsystem models are created within `RunSimulation` while others are created by independent functions called by `RunSimulation`. The plant consists of the dynamics of the spacecraft structure derived from a finite element model. The main distur-

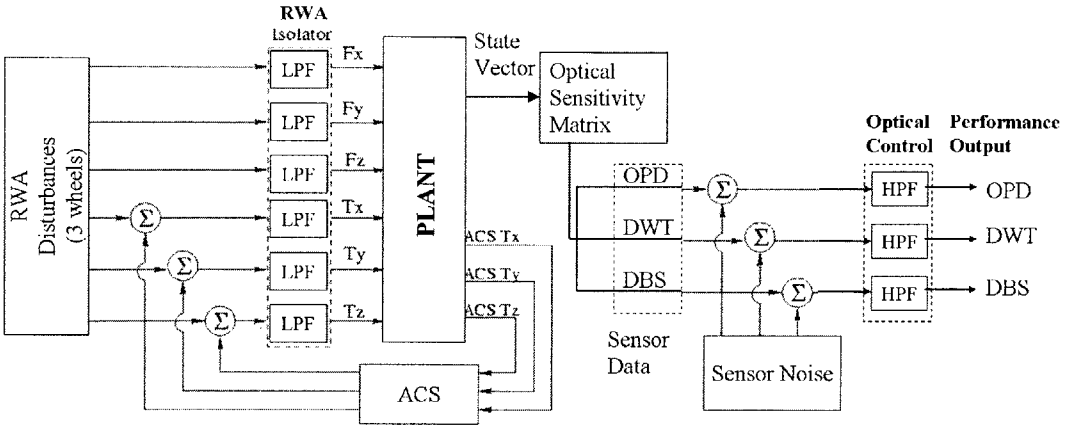

Figure 1-7: Block diagram of integrated model

bance input to the plant comes from the reaction wheel imbalances. A stochastic broadband reaction wheel disturbance model passes through a low-pass filter isolator before entering the plant. A linear optical sensitivity matrix (`Cmatrix` from above) is generated using the CODE-V® optical modeling software. The sensitivity matrix relates the motion of critical nodes in the finite element model to the desired optical performance metrics. Optical sensor noise is added to the performance outputs before they enter the optical controllers (modeled as high-pass filters). The output of the optical controllers is optical performance.

The body of the thesis will begin in Chapter 2 with a broad overview of the mathematics behind our integrated modeling method. This will provide a solid foundation from which we can build up the subsystem models in the proceeding chapters. In Chapter 7 we will explain the different performance analysis methods. In Chapter 8 we will wrap up the thesis with conclusions and recommendations for future work.

Chapter 2

Model Overview

This chapter will give an overview of the integrated modeling method we will use to generate our model of TPF. It will provide the mathematical foundation for the core sections of the model and explain the framework that is used to expand the integrated model.

The minimum configuration of our integrated model contains a structural dynamics model and an optical model. Performance is measured by applying a disturbance to the structure and calculating the effect on optical output metrics. Therefore, the four core components needed to find optical performance are a structural dynamics model, optics model, disturbance model, and a performance analysis method.

2.1 Structural Dynamics Model

This section will give an overview of the method used to create a multi-degree-of-freedom structural dynamics model. The way that this method is applied and the details of our specific TPF structure will be explained in Chapter 3.

The method begins by first generating the model in the time domain with physical coordinates in second order form. It is then transformed into modal coordinates so that modal damping may be added. The modal, time domain model is then converted into state-space, first order form so that it may be linked to other components of the integrated model.

2.1.1 Time Domain Model

The dynamics of a multi-degree-of-freedom system are described in the time domain by the following equation:

$$\mathbf{M}\ddot{\mathbf{x}} + \mathbf{K}\mathbf{x} = \mathbf{f}. \tag{2.1}$$

Both **M** and **K** are n x n square matrices where n is the number of degrees of freedom in the system. The mass matrix, **M**, contains the masses or inertias associated with each degree of freedom. The stiffness matrix, **K**, is populated by terms representing conservative resistance to motion about each degree of freedom. The motion of each degree of freedom is described by the elements contained in the n x 1 vector **x**. The input to the system is through a vector of forcing functions, **f**.

The structure can be represented by a multi-degree-of-freedom finite element model (FEM). The finite element analysis software uses the information in the bulk data deck to generate the mass and stiffness matrices. It then calculates the eigenvectors and eigenvalues of the system by solving the equation

$$[\mathbf{K} - \lambda\mathbf{M}]\Phi = 0. \tag{2.2}$$

The eigenvectors in the matrix, Φ, define the mode shapes of the system. The elements of the diagonal eigenvalue matrix, λ, give the natural frequencies by the relation

$$\lambda_{i,i} = \omega_i^2 \tag{2.3}$$

where ω_i is the natural frequency of mode i. The terms λ and ω^2 will be used interchangeably to represent the diagonal eigenvalue matrix. Meirovitch [25] gives a good overview of dynamic systems and explains that by orthogonality

$$\Phi_j^T \mathbf{M} \Phi_i = 0 \tag{2.4}$$

and

$$\Phi_j^T \mathbf{K} \Phi_i = 0 \tag{2.5}$$

for $j \neq i$. Since $\omega^2 = \mathbf{M}^{-1}\mathbf{K}$, we also have the relation

$$\Phi^T \mathbf{K} \Phi = \omega^2 \Phi^T \mathbf{M} \Phi. \tag{2.6}$$

The solution to Equation 2.1 can be found using the principal of superposition. Equation 2.7 shows that any vibration of our multi-degree-of-freedom system can be described as a linear combination of vibrations of each mode.

$$\mathbf{x} = \sum_{i=1}^{n} q_i \Phi_i \tag{2.7}$$

Each mode is a simple harmonic oscillator

$$q_i(t) = C_i \cos(\omega_i t + \phi_i) \tag{2.8}$$

with frequency, ω_i. The amplitude, C_i and phase, ϕ_i of each mode would be determined by initial conditions. In matrix form, the superposition of Equation 2.7 is written as a transformation from physical coordinates, $\mathbf{x}$, to modal coordinates, $\mathbf{q}$:

$$\mathbf{x} = \Phi \mathbf{q}. \tag{2.9}$$

Substituting Equation 2.9 into the original second order form of Equation 2.1 and multiplying through by Φ^T we arrive at

$$\Phi^T \mathbf{M} \Phi \ddot{\mathbf{q}} + \Phi^T \mathbf{K} \Phi \mathbf{q} = \Phi^T \mathbf{f}. \tag{2.10}$$

Applying the relationship from Equation 2.6, Equation 2.10 becomes

$$\Phi^T \mathbf{M} \Phi \ddot{\mathbf{q}} + \omega^2 \Phi^T \mathbf{M} \Phi \mathbf{q} = \Phi^T \mathbf{f}. \tag{2.11}$$

The output eigenvectors from a finite element analysis are typically mass normalized so that

$$\Phi^T \mathbf{M} \Phi = I. \tag{2.12}$$

Applying Equation 2.12, Equation 2.11 reduces to

$$\ddot{\mathbf{q}} + \omega^2 \mathbf{q} = \Phi^T \mathbf{f}. \tag{2.13}$$

By representing the dynamics of the system in modal form in Equation 2.13, we have created a set of elastically and inertially uncoupled equations of motion. This is useful because it provides us an easy way to add damping. Whereas the stiffness matrix relates forces to displacements, damping is modeled as a nonconservative resistive force proportional to the velocity of each degree of freedom. In this case, the resistive forces are proportional to the velocity of the modal degrees of freedom, $\dot{\mathbf{q}}$. With the addition of modal damping, Equation 2.13 becomes

$$\ddot{\mathbf{q}} + 2\zeta\omega^2 \dot{\mathbf{q}} + \omega^2 \mathbf{q} = \Phi^T \mathbf{f} \tag{2.14}$$

where ζ is the modal damping ratio.

2.1.2 State-Space Representation/Optical Model

The time domain model with modal coordinates is converted to state-space form for two main reasons. The first is for the ease of linking independent models in order to create a large integrated model of a complex system like TPF. The second is to utilize the output equation that relates the motion of physical points in the structure to the desired performance metrics. This output equation will be used to implement the optics model.

A state-space model consists of a set of first-order differential equations written in a standard, compact matrix form. The state equation is given by

$$\dot{x} = Ax + Bu \tag{2.15}$$

where x is the state vector, A is the system matrix, u is the input vector, and B is

the input pointing matrix. The output equation is

$$y = Cx + Du. \tag{2.16}$$

In controls applications, D would be a feed through term from input directly to output. However, for most structural dynamics models $D = 0$. The C matrix is essentially a scaling matrix relating the motion of the physical states in x to the desired output measurements, y. In our TPF model, the C matrix will relate the motion of the mirrors to certain optical performance metrics. Chapter 4 will cover the C matrix generation through the use of the optical model.

Our multi-degree-of-freedom system is represented in the state-space domain by converting Equation 2.14 into

$$\dot{\hat{q}} = A\hat{q} + Bu \tag{2.17}$$

with the output equation

$$y = C\hat{q}. \tag{2.18}$$

The state vector is

$$\hat{q} = \left\{ \begin{array}{c} \mathbf{q} \\ \dot{\mathbf{q}} \end{array} \right\}, \tag{2.19}$$

and the system matrix is

$$A = \left(\begin{array}{cc} 0 & I \\ -\omega^2 & -2\zeta\omega \end{array} \right). \tag{2.20}$$

The vector u is the forcing input term. It will apply the disturbance input, f, from Equation 2.14. The pointing vector is

$$B = \left(\begin{array}{c} 0 \\ \Phi^T \end{array} \right). \tag{2.21}$$

With all these components substituted into Equation 2.17, we arrive at

$$\begin{Bmatrix} \dot{\mathbf{q}} \\ \ddot{\mathbf{q}} \end{Bmatrix} = \begin{pmatrix} 0 & I \\ -\omega^2 & -2\zeta\omega \end{pmatrix} \begin{Bmatrix} \mathbf{q} \\ \dot{\mathbf{q}} \end{Bmatrix} + \begin{pmatrix} 0 \\ \Phi^T \end{pmatrix} u. \tag{2.22}$$

We now have our structure fully modeled in state-space form. Individual state-space models can be connected by setting the output of one model to be an input in the adjoining model. Once all the models are linked together, one large state-space model will have been created that can synthesize the effects of many different sub-components on the global performance metrics.

2.2 Disturbance Modeling/Performance Analysis

We are now close to being able to perform our disturbance analysis and predict the performance of our system. It is difficult, however, to create forcing functions in the time domain that accurately model the disturbances that a spacecraft such as TPF is likely to encounter during its normal operations. As will be covered in Chapter 5, the main disturbance source on most spacecraft is caused by imbalance in the reaction wheels. The forces and torques from reaction wheels will vary depending on the range of speeds under which the wheel is currently operating. The speed range is in turn determined by a variety of factors including the time since the last momentum dump and variation in external disturbances such as solar pressure and gravitational torque. In addition, reaction wheel assemblies (RWAs) are typically designed for redundancy. As such, attitude adjustments may be performed by any combination of wheels with overlapping torque authority, further adding to the ambiguity of expected wheel speeds.

Recent work has shown that due to this time domain variability, reaction wheel disturbances can be more easily modeled in the frequency domain as power spectral density (PSD) functions [26] [23]. Therefore, in order to utilize this PSD disturbance source, we must move our state-space model into the frequency domain. First, we

take the Laplace Transform of Equation 2.17:

$$\hat{Q}(s)s = A\hat{Q}(s) + BU(s). \tag{2.23}$$

Rearranging Equation 2.23 we find that

$$\hat{Q}(s) = (sI - A)^{-1}BU(s). \tag{2.24}$$

The Laplace Transform of Equation 2.18 is

$$Y(s) = CQ(s). \tag{2.25}$$

Substituting Equation 2.24 into Equation 2.25 we find that

$$Y(s) = C(sI - A)^{-1}BU(s). \tag{2.26}$$

Now, the transfer function of disturbance input to performance output is found:

$$G(s) = U(s)^{-1}Y(s) = C(sI - A)^{-1}B. \tag{2.27}$$

As shown in Brown and Hwang [3], the output PSD of a transfer function with PSD input $S_U(s)$ is

$$S_Y(s) = G(s)S_U(s)G^H(s) \tag{2.28}$$

where $G^H(s)$ is the "Hermetian", or complex conjugate transpose, of $G(s)$. An effective way of measuring performance is to find the root-mean-square (RMS) of the output PSD. The mean-square value is first found by

$$\sigma_Y^2 = E(Y^2) = \frac{1}{2\pi j}\int_{-j\infty}^{j\infty} S_Y(s)ds. \tag{2.29}$$

This is the same as taking the variance of the output since ours is a zero-mean system [31]. The RMS is found by taking the square root of the mean-square value. We now

have a complete method by which to analyze the performance of our multi-degree-of-freedom system.

Chapter 3

Structural Model

The first model component we will cover is the structure, or "plant". Figure 3-1 shows the plant highlighted in the middle of the block diagram. Inputs to the plant are the filtered reaction wheel disturbances. The output from the plant is the state vector. Some of these states will be used as Attitude Control System sensor values while others are multiplied by the optical sensitivity matrix.

As explained in Chapter 1, TPF is still in its early development phase and many changes are expected to be made in the design of the structure. Changes are likely in the size, shape and material properties of the truss as well as in the optical prescription of the telescopes. It is therefore important that any FEM of TPF can be easily regenerated with changes in a wide variety of parameters. This way, the model will be able to accommodate changes in the design over time as well as be used in the trade analyses that help determine new designs.

Using design variability as a motivation, MATLAB code was written that automatically generates the FEM bulk data deck, runs the finite element analysis and extracts the eigenvectors and eigenvalues to build the state-space structural dynamics model. This MATLAB code begins with two functions, `TPF_Truss_Model` and `Mirrorfunction`, that are called by `RunSimulation`. Elements of `DesignVector` and `ConstantsVector` are used to generate arrays describing grid point locations, element connectivity, and material properties for both the truss and the mirrors. A third MATLAB function, `WriteDAT`, uses the arrays generated from the previous two

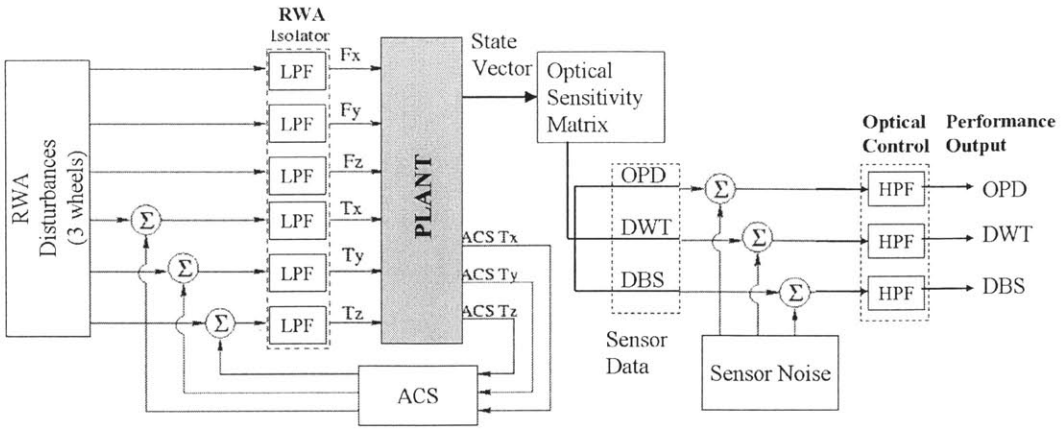

Figure 3-1: Integrated model with structural "Plant" block highlighted

functions to write out the bulk data deck "`.dat`" file that can be read by NASTRAN®.

MATLAB then calls NASTRAN to run the finite element analysis. A pair of simple PERL scripts are used to extract the eigenvectors, eigenvalues and mass properties from the NASTRAN "`.f06`" output file. Then, following the method described in Chapter 2, the eigenvectors and eigenvalues are used to generate equations of motion of the system in modal form. Modal damping is added to the equations of motion. The modal damping ratio is a parameter in the `ConstantsVector` and has a nominal value of $\zeta = 0.001$. The fully assembled finite element model is shown in Figure 3-2.

3.1 Truss Generation

As explained in Chapter 1, `ConstantsVector` and `DesignVector` contain all the parameters that are used in the generation of the entire integrated model. Tables 3.1 and 3.2 list the elements of `ConstantsVector` and `DesignVector` that are used in the truss generation as well as their nominal values. For our analysis, we use aluminum material properties for the truss. Aluminum will not necessarily be used in the final design for TPF but it is a good place to start. One area of possible design modification is in the shape of the truss bays and the cross-sectional area of the truss elements. To accommodate this, the height, width, and radius parameters are actually vectors

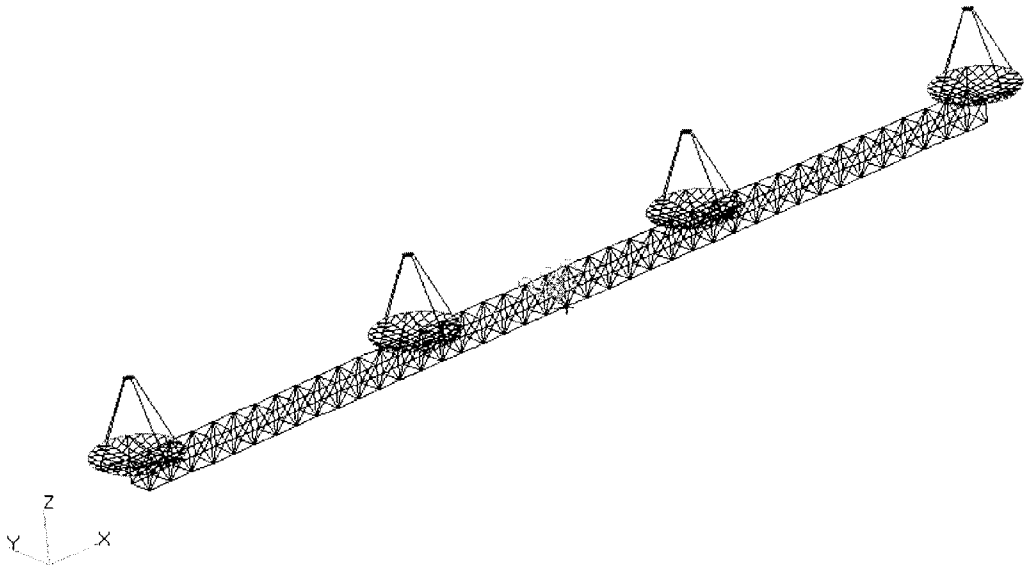

Figure 3-2: Full finite element model

Table 3.1: Truss ConstantsVector

Parameter (units)	Nominal Value
Baseline length (m)	40
Number of apertures	4
Combiner mass (kg)	430
Bus mass (kg)	520
Reaction wheel mass (kg)	10.8
Frequency upper limit (Hz)	278
Modal damping ratio	0.001

that can be given a different value for each bay in the truss. Nominally, these values are constant across the truss. The finite element analysis is limited to modes between 0-278 Hz. This is done so that the structural model has the same frequency range as the reaction wheel disturbance model.

Based on the input parameters, the MATLAB code first generates the coordinates for the nodes of the truss. These will be the grid points in the finite element model. In the nominal case, the truss is modeled as having one meter per side cubic bays. Truss members are generated by connecting appropriate grid points with circular cross-section "CBAR" elements. Longerons and battens are used to create the edges

Table 3.2: Truss DesignVector

Parameter (units)	Nominal Value
Number of bays	40
Element radius vector (m)	0.01016
Bay width vector (m)	1
Bay height vector (m)	1
Truss material density (kg/m^3)	2800
Truss material modulus (N/m^2)	72×10^9

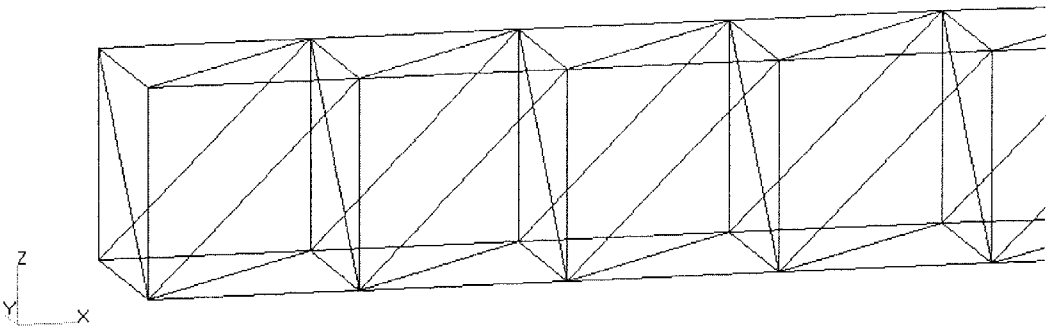

Figure 3-3: Zoomed in view of truss section

of the cube and a diagonal element is placed on each face of the cube to rigidify the truss. Each bay will have 8 unique elements and share 5 elements with each of its neighbors. The only exceptions are the bays at the two ends of the truss. The end bays will have only one neighbor sharing truss elements. Figure 3-3 shows a section of the truss with all the longerons, battens and diagonal elements. The MATLAB truss generation code is written in such a way so that the truss will always be symmetric about its central y-z plane. This means that any variation in truss bay geometry will be applied symmetrically on both sides of the truss.

The spacecraft bus and optics combiner are represented as point masses at the center of the truss. They are at a point where x=0 and y=0.5 m (for a 1 m bay). Figure 3-4 shows the z-location of each point mass and how they are connected to the rest of the truss. The reaction wheel assembly (RWA) is located at the bottom, z=0 m, and is attached to the 6 circled points at the top of the truss with a rigid body

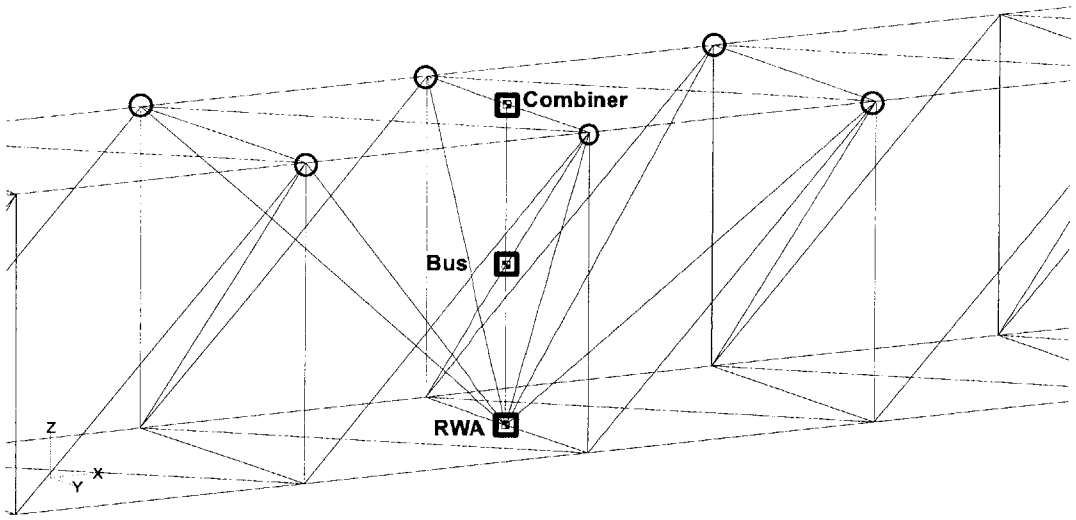

Figure 3-4: Point mass locations in the truss

element ("RBE2"). The spacecraft bus is located halfway up the truss at z=0.5 m. The bus is attached to the RWA with a "RBAR" rigid body element. The combiner, at z=1 m, is in turn attached to the spacecraft bus through another "RBAR" rigid body element.

3.2 Mirror Generation

The elements of `ConstantsVector` and `DesignVector` that are used in the mirror generation are listed in Tables 3.3 and 3.4 along with their nominal values. Beryllium is used for the nominal material properties of the mirrors. In `ConstantsVector`, the mirror thickness is derived from the mirror density in order to give an areal density of 15 kg/m^2. This is the lightweight optics goal described in Chapter 1 that will be demonstrated by JWST and used on TPF. The mirror modulus is listed in `DesignVector` since the mirror backing structure has not yet been determined. Likely, some sort of honeycomb stiffening structure will be attached to the back of the mirror that will give the mirror an equivalent stiffness greater than that of beryllium. In fact, the modulus will be stiffened by a factor of 100 for both the mirror and the

Table 3.3: Mirror ConstantsVector

Parameter (units)	Nominal Value
Mirror density, ρ (kg/m^3)	1850
Mirror thickness (m)	$15/\rho$
Mesh resolution	6

Table 3.4: Mirror DesignVector

Parameter (units)	Nominal Value
Mirror modulus (N/m^2)	300×10^9
Support modulus (N/m^2)	72×10^9
Support density (kg/m^3)	2800
Pri. mirror diameter (m)	3.5
Pri. mirror radius of curvature (m)	7
Pri. mirror conic constant	-0.9999964
Sec. mirror diameter (m)	0.4
Sec. mirror radius of curvature (m)	-0.4076273
Sec. mirror conic constant	-0.9999393

mirror mounts in Chapter 7. This is done to make the dynamics of the mirror modes more realistic. The rest of the elements in these tables will be explained as they come up throughout this section.

The x-y coordinates of each primary and secondary mirror are generated based on the mirror diameter and mesh resolution. A method is employed to produce grid points that will result in relatively isometric "`CQUAD8`" and "`CTRIA6`" elements. Two input parameters are necessary for mirror x-y mesh generation. These parameters are mirror diameter, `D`, and mesh resolution, `res`. The value of `res` defines the number of element edges along each of the four radii aligned with the x and y axes. Figure 3.2 shows a mirror with a mesh resolution of `res=6`. The following Matlab code generates the grid points for the upper-right quadrant of the mirror.

```
r=D/2;
thstep=pi/2/res;
dr=r/res;
for n=0:(res-1)
   th=pi/2-thstep*n;
   dx=(r*cos(th)-dr*n)/(res-n);
```

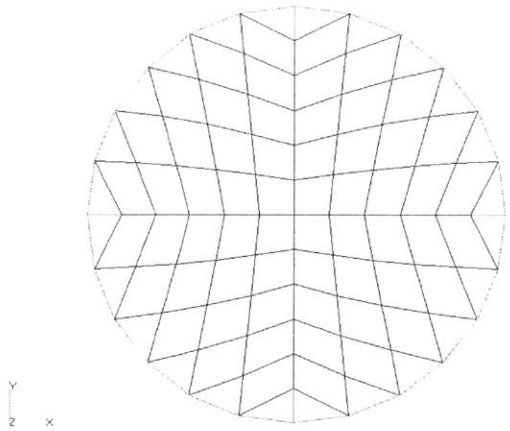

Figure 3-5: Mirror mesh x-y coordinates

```
        dy=(r*sin(th))/(res-n);
        for m=0:(res-n)
            grdpt(k,1:2)=[dx*m+n*dr dy*m];
            k=k+1;
        end;
    end;
```

The grid points for the upper-left quadrant are found by reflecting the upper-right grid points about the y-axis. The full upper-half grid points can then be reflected about the x-axis to complete the x-y grid point mesh.

The mirror is given its 3 dimensional shape by calculating the z-coordinate for each grid point. This shape is based upon the optical prescription for the mirror. The optical prescription parameters are radius of curvature, R and its conic constant, K. The z coordinate for each grid point is given as a function of the radial distance from the center, r:

$$z(r) = \frac{cr^2}{1 + \sqrt{1 - (1+K)c^2r^2}}, \tag{3.1}$$

where $r = \sqrt{x^2 + y^2}$ and $c = \frac{1}{R}$ [1].

Each primary mirror is assumed to be identical and each secondary mirror is assumed to be identical. Each primary mirror is attached to the four closest truss

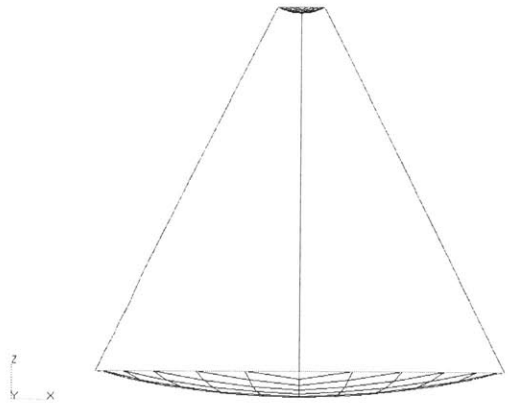

Figure 3-6: Aperture: primary and secondary mirrors

nodes through a hexapod kinematic mount. A kinematic mount is defined as

> *A mount for an optic element or optics assembly, designed so that all six degrees of freedom are singly constrained. This assures that movement will be prevented, while stress will not be introduced into the optics* [20].

Each secondary mirror is attached to its primary mirror with four "`CBAR`" elements equally spaced around the perimeter of the mirrors. The material properties for both the kinematic mount and the secondary mirror supports are defined by the "support" properties in `DesignVector`. Figure 3-6 shows a connected primary and secondary mirror.

3.3 Model Fidelity

In any design process, certain decisions must be made as to what level of fidelity should be used. These decisions are based upon the purpose that the model will serve and how much is known about the environments in which the modeled object will operate. For example, it would be useless to model thermal expansion properties in our TPF model if we do not know the expected temperature ranges that TPF will encounter. Also, depending on the level of accuracy required, less complicated "representative"

models are sometimes used to determine broad dynamic characteristics before the more detailed models are created.

The first iteration of the TPF structural model used a beam to model the properties of the truss. Four point masses were evenly spaced along the beam to represent each of the telescopes and two point masses were placed in the center of the beam to represent the combiner and bus. This level of complexity was good enough for the beginning stages of the integrated model but higher fidelity was needed to capture all of the effects we wanted. The full truss was needed for more accurate mode shapes in the higher frequencies. The fully-modeled primary and secondary mirrors allowed for the addition of differential wavefront tilt and differential beam shear performance metrics as well as improved optical pathlength difference calculations.

Our iterative upgrades in the structural model demonstrate the modularity of the integrated model. While altering the structural model, the inputs were always kept the same. Since this was done, no changes were needed in the RWA disturbance model. However, additional outputs were added to the structural model. This was necessary for the calculation of the new performance metrics.

The current structural model still uses point masses to represent the combiner and bus. These are areas that will likely be modeled in more detail as more is known about their design and higher fidelity performance models are needed. Other components that might be included in later models of the structure are flexible appendages such as solar arrays, sun shields and antennas.

Chapter 4

Optical Model

Once the FEM is generated, a sensitivity matrix is needed to relate the motions of critical nodes to optical performance metrics. The TPF interferometer is modeled as four separate apertures using CODE-V. Each aperture's optics train consists of a primary mirror, secondary mirror, fold mirrors and an image plane. A MATLAB/CODE-V interface is used to apply perturbations to the mirrors and to retrieve ray trace data.

In this chapter we will provide an overview of the optical layout, explain the optical performance metrics and derive the partial derivatives relating the motion of critical nodes in the FEM to these performance outputs. These partial derivatives are used to assemble the optical sensitivity matrix whose block is highlighted in Figure 4-1.

4.1 Optical Layout

The layout of each aperture consists of a primary mirror, secondary mirror, fold mirrors and an image plane. The optical prescription defining the primary mirrors for each aperture is identical and the optical prescription for each secondary mirror is identical. The fold mirrors are arranged in such a way to direct the light towards the center of the spacecraft and create equal pathlengths for each aperture.

Figure 4-2 shows a ray trace through the optical layout for aperture one. The light comes in through the top, and first hits the primary mirror. The light is then focused onto the secondary mirror which in turn collimates and reflects the light towards the

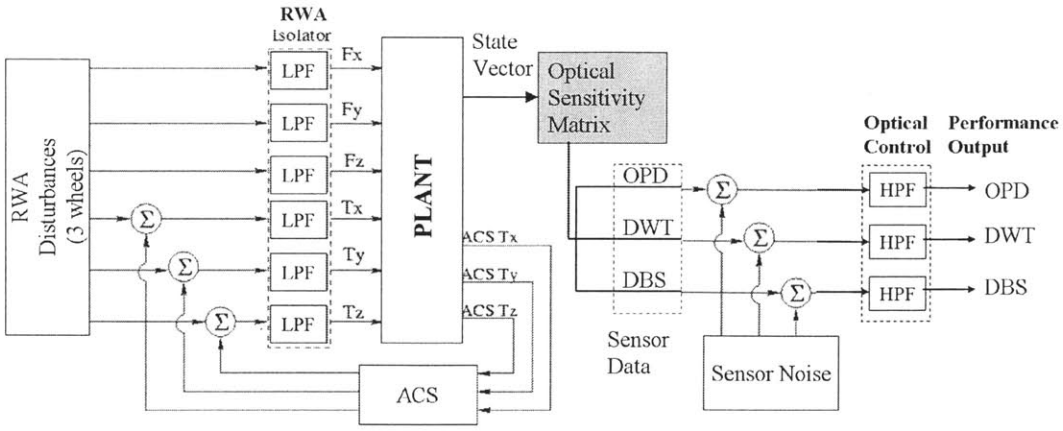

Figure 4-1: Integrated model block diagram with optical sensitivity matrix block highlighted

first fold mirror. Fold mirror one redirects the light by 90° and sends it on a 20 m trip towards the center of the spacecraft where the combiner optics will reside. Since details of the combiner are not needed for our performance metrics, the combiner is simply modeled as a fold mirror that redirects the light towards a common image plane.

Because aperture two is closer to the center of the spacecraft, its optical layout is slightly different. The columnated light beam must first travel beyond the center of the spacecraft and bounce off an additional fold mirror at the location of aperture three. This extra bounce allows for the full 20 m pathlength. Figure 4-3 shows the optical layout for aperture two. After the light hits fold mirror two, it bounces back towards the center of the spacecraft where it is redirected to the image plane by fold mirror three.

Due to the symmetry of the spacecraft, the layout of aperture three is a mirror image of that for aperture two. Likewise, the layout of aperture four is a mirror image of the layout for aperture one. These four optical models will be used to calculate the optical performance sensitivities.

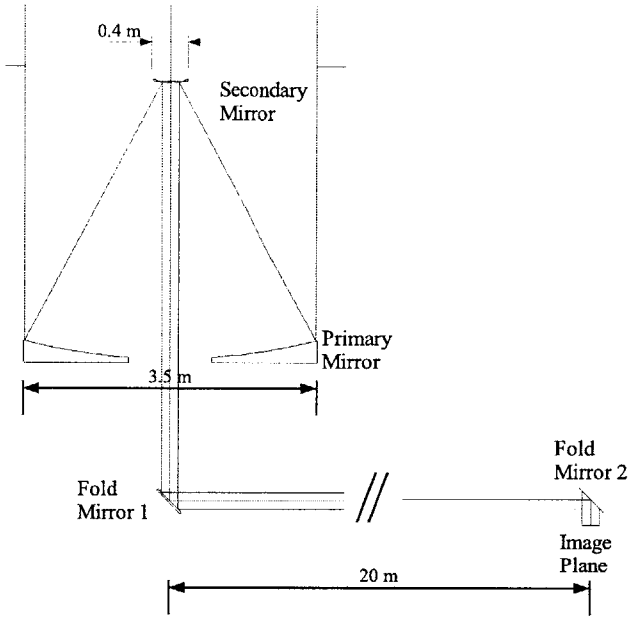

Figure 4-2: Optical layout of aperture one.

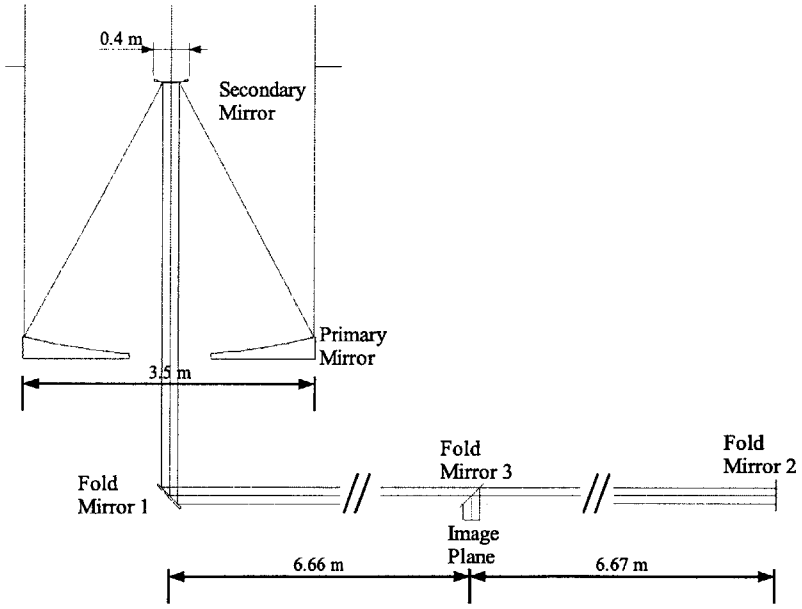

Figure 4-3: Optical layout of aperture two.

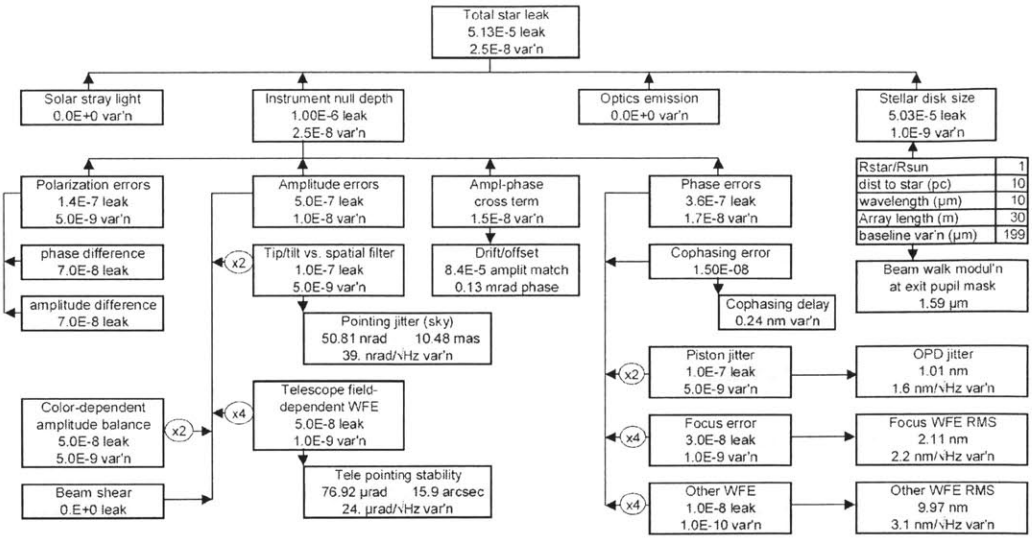

Figure 4-4: Possible error budget flow down chart [4].

Table 4.1: Nominal performance requirements.

Performance Metric	Requirement
OPD	1.01 nm
DWT	50.81 nrad
DBS	1.59 μm

4.2 Optical Performance Metrics

When modeling any spacecraft, relevant metrics must be assigned to accurately predict performance. These metrics are used to verify that mission requirements will be met, or to help in the redesign process if it is found that the mission requirements will not be met.

As explained in Chapter 1, the main optical requirements for TPF are Null Depth and Null Stability. Therefore, a flow-down is performed to determine the requirements on factors that contribute to Null Depth and Null Stability degradation. An example of a possible flow-down is shown in Figure 4-4. Although exact requirements have not yet been set, we will use the values of "OPD jitter," "pointing jitter," and "beam walk modulation" from this chart to set the requirements for OPD, DWT, and DBS in our analysis. The values from the chart give us the requirements shown in Table 4.1.

In this model, we will focus on the contributing factors of Optical Pathlength Difference (OPD), Differential Wavefront Tilt (DWT) and Differential Beam Shear (DBS). First, OPD is the difference in pathlength between two apertures. In order for interferometry to occur, all pathlengths must be equal to within a small fraction of the wavelength of light being observed. Secondly, the angles at which the light from different apertures hit the image plane must also be closely aligned. The measurement of error in this angular alignment is known as DWT. If there is significant DWT, the centerline may have zero OPD while OPD across the wavefront cross-section will grow as a function of distance from the center line. Lastly, DBS measures the error in overlap of beams from different apertures. Beams must overlap almost perfectly for optimal optical performance. If there is too much beam shear, not only will interferometry break down but the image that does come through will become blurry. The effect of disturbances on the spacecraft will be measured by OPD, DWT and DBS.

4.3 Partial Derivative Methods

A linear optical model must be created to relate the motion of nodes in the finite element model to the performance outputs. The linear sensitivities (or partial derivatives) are obtained by using the three step process described by Howard [15].

1. Perturb a single degree of freedom by a small representative value in the range expected due to the modeled disturbances.

2. Extract data from a ray trace to determine the optical performance metric.

3. Divide the performance metric by the magnitude of the perturbation to find the partial derivative.

This method is implemented through a set of MATLAB functions that interface with CODE-V. One MATLAB function computes the pathlength derivatives, the second finds the Wavefront tilt derivatives, and the last calculates the beam shear derivatives.

Inputs to the MATLAB functions include the CODE-V file name, the number of mirrors, the coordinates of the ray to be traced, the magnitude of the linear and rotational perturbations, and the static tilt for each mirror.

4.3.1 Pathlength Sensitivity

The Matlab function that calculates pathlength sensitivity is called "`PL_deriv`." The ray input coordinates for `PL_deriv` should be at the center of the primary mirror (x=0, y=0). The function first tells CODE-V to perform a ray trace through every surface in the optics train and calculate the total nominal pathlength. Next, each mirror is perturbed a small amount in each of its six degrees of freedom. After each perturbation, the new total pathlength is calculated. The difference between the perturbed pathlength and the nominal pathlength is divided by the magnitude of the perturbation to find the partial derivative of change in pathlength over change in each degree of freedom. Before each degree of freedom is perturbed, the previous perturbation is removed so that the optics train is back at its nominal state. The output of `PL_deriv` is an n x 6 matrix of partial derivatives where n is the number of mirrors along the optics train.

The total pathlength for a given aperture, i, is

$$\Delta PL_i = \sum_{j=1}^{n} \frac{\delta PL_{i,j}}{\delta Q_{i,j}} Q_{i,j} \tag{4.1}$$

where

$$\frac{\delta PL_{i,j}}{\delta Q_{i,j}} = \left(\begin{array}{cccccc} \frac{\delta PL_{i,j}}{\delta x_{i,j}} & \frac{\delta PL_{i,j}}{\delta y_{i,j}} & \frac{\delta PL_{i,j}}{\delta z_{i,j}} & \frac{\delta PL_{i,j}}{\delta \alpha_{i,j}} & \frac{\delta PL_{i,j}}{\delta \beta_{i,j}} & \frac{\delta PL_{i,j}}{\delta \gamma_{i,j}} \end{array} \right), \tag{4.2}$$

and $Q_{i,j}$ is a vector describing the motion about all six degrees of the critical node for mirror j in aperture i:

$$Q_{i,j} = \left(\begin{array}{cccccc} x_{i,j} & y_{i,j} & z_{i,j} & \alpha_{i,j} & \beta_{i,j} & \gamma_{i,j} \end{array} \right)^T. \tag{4.3}$$

The translational degrees of freedom are x, y, and z. The rotational degrees of freedom are the angles α, β, and γ about x, y, and z, respectively.

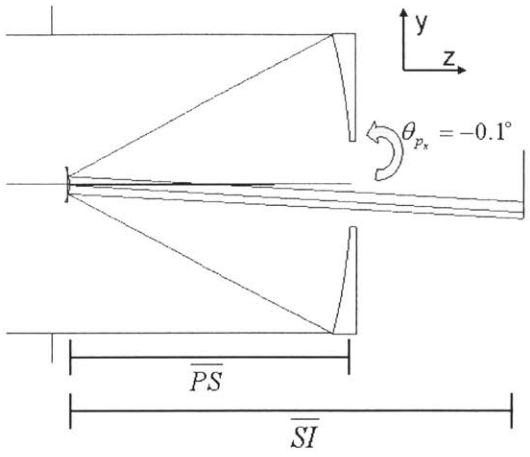

Figure 4-5: Ray trace with tilt perturbation in primary mirror

4.3.2 Wavefront Tilt Sensitivity

The function "`WT_deriv`" calculates the wavefront tilt sensitivities. Since the tilt must be measured about two axes, the function must be run twice. It is run once with an input ray at (x=1, y=0) to detect rotations about the y-axis and once with the input ray at (x=0, y=1) to detect rotations about the x-axis. The x,y values are scaled by the primary mirror radius. Figure 4-5 gives an example of an exaggerated tilt perturbation. In this image, the primary mirror is rotated by 0.1° and the effect on the ray trace can be seen. The tilt in the primary mirror causes a change in trajectory of the reflected light. This change in trajectory causes the light to hit the image plane at a skewed angle (wavefront tilt) and a new location (beam shear). The distances $\overline{PS}$ and $\overline{SI}$ will be used later to check the CODE-V results.

Like before, the nominal pathlength is first calculated before any perturbations are applied. After each perturbation, the angle of the beam is found by dividing the change in pathlength by the radius of the beam at the image plane. This value is then divided by the magnitude of the perturbation to find the partial derivative. Again, the output of this function is an n x 6 matrix of partial derivatives where n is the number of mirrors along the optics train.

The total wavefront tilt for a given aperture, i, is

$$\Delta WT_i = \sum_{j=1}^{n} \frac{\delta WT_{i,j}}{\delta Q_{i,j}} Q_{i,j} \tag{4.4}$$

where

$$\frac{\delta WT_{i,j}}{\delta Q_{i,j}} = \left(\begin{array}{cccccc} \frac{\delta WT_{i,j}}{\delta x_{i,j}} & \frac{\delta WT_{i,j}}{\delta y_{i,j}} & \frac{\delta WT_{i,j}}{\delta z_{i,j}} & \frac{\delta WT_{i,j}}{\delta \alpha_{i,j}} & \frac{\delta WT_{i,j}}{\delta \beta_{i,j}} & \frac{\delta WT_{i,j}}{\delta \gamma_{i,j}} \end{array} \right). \tag{4.5}$$

4.3.3 Beam Shear Sensitivity

Finally, "`BS_deriv`" is used to calculate the beam shear sensitivities. Rather than measuring the pathlength, this function determines the location of a given ray on the image plane. In the nominal state, a commanded ray of (x=0, y=0) will fall on the image plane at the origin (x=0, y=0). Linear and rotational perturbations of the mirrors will cause this beam to shear and change its x,y location on the image plane.

`BS_deriv` calculates the change in x and y location and divides this by the perturbation to find the partial derivatives for each. The resulting output is a matrix twice as large as before. The matrix is n x 12 since there are 6 partial derivatives for both the x location and y location.

The total beam shear for a given aperture, i, is

$$\Delta BS_i = \sum_{j=1}^{n} \frac{\delta BS_{i,j}}{\delta Q_{i,j}} Q_{i,j} \tag{4.6}$$

where

$$\frac{\delta BS_{i,j}}{\delta Q_{i,j}} = \left(\begin{array}{cccccc} \frac{\delta BS_{i,j}}{\delta x_{i,j}} & \frac{\delta BS_{i,j}}{\delta y_{i,j}} & \frac{\delta BS_{i,j}}{\delta z_{i,j}} & \frac{\delta BS_{i,j}}{\delta \alpha_{i,j}} & \frac{\delta BS_{i,j}}{\delta \beta_{i,j}} & \frac{\delta BS_{i,j}}{\delta \gamma_{i,j}} \end{array} \right). \tag{4.7}$$

4.4 CODE-V Mirror Rotations

This section explains the way that CODE-V applies perturbations and derives the coordinate transformations for the rotational perturbations. CODE-V allows surfaces to be decentered translationally along x, y, and z and rotationally by angles, α, β, and γ in that order. A positive α rotation is a right hand rotation about the

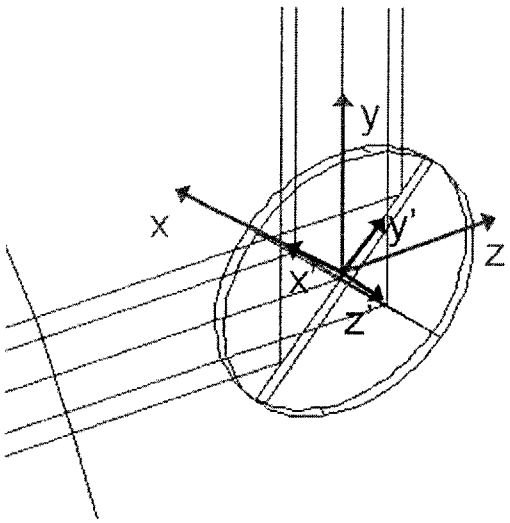

Figure 4-6: Fold mirror body axes rotated from global axes

negative x axis, a positive β rotation is a right hand rotation about the negative y axis and a positive γ rotation is a right hand rotation about the positive z axis [13]. Since some of the mirrors have nominal rotations, rotations about the global axes do not necessarily equate to rotations about the mirror's body axes. A coordinate transformation scheme is necessary to convert a rotation about a single global axis to a rotation about multiple body axes.

Figure 4-6 depicts a fold mirror with a nominal rotation of $\alpha' = -45°$. Rotations in the global frame are α, β, and γ about X, Y and Z. Rotations in the body frame are α', β', and γ' about X', Y', and Z'. The X', Y' plane is coplanar with the fold mirror surface. The Z' axis is directed out the back of the mirror. X and X' are collinear.

Using the Euler rotation theorem, the global rotations are transformed to body rotations through the following matrix:

$$M = \begin{bmatrix} \cos\gamma'\cos\alpha' - \cos\beta'\sin\alpha'\sin\gamma' & \cos\gamma'\sin\alpha' + \cos\beta'\sin\alpha'\sin\gamma' & \sin\gamma'\sin\beta' \\ -\sin\gamma'\cos\alpha' - \cos\beta'\sin\alpha'\cos\gamma' & -\sin\gamma'\sin\alpha' + \cos\beta'\cos\alpha'\cos\gamma' & \cos\gamma'\sin\beta' \\ \sin\beta'\sin\alpha' & -\sin\beta'\sin\alpha' & \cos\beta' \end{bmatrix} \tag{4.8}$$

where

$$\begin{pmatrix} \Delta\gamma' \\ \Delta\beta' \\ \Delta\alpha' \end{pmatrix} = M \begin{pmatrix} \Delta\gamma \\ \Delta\beta \\ \Delta\alpha \end{pmatrix} \tag{4.9}$$

and $\Delta\alpha$, $\Delta\beta$, and $\Delta\gamma$ are small, differential rotations.

In our case, $\gamma' = 0$ since the mirror is symmetric about Z'. This reduces M to

$$M = \begin{bmatrix} \cos\alpha' & \sin\alpha' & 0 \\ -\cos\beta'\sin\alpha' & \cos\beta'\cos\alpha' & \sin\beta' \\ \sin\beta'\sin\alpha' & -\sin\beta'\sin\alpha' & \cos\beta' \end{bmatrix}. \tag{4.10}$$

Inserting Equation 4.10 into 4.9 we find that

$$\Delta\gamma' = \Delta\gamma\cos\alpha' + \Delta\beta\sin\alpha' \tag{4.11}$$

$$\Delta\beta' = -\Delta\gamma\cos\beta'\sin\alpha' + \Delta\beta\cos\beta'\cos\alpha' + \Delta\alpha\sin\beta' \tag{4.12}$$

$$\Delta\alpha' = \Delta\gamma\sin\beta'\sin\alpha' - \Delta\beta\sin\beta'\sin\alpha' + \Delta\alpha\cos\beta' \tag{4.13}$$

In our model, $\beta' = 0$ for all fold mirrors. Considering this and remembering that no rotation about Z' is necessary (due to symmetry), we find that the rotational perturbations ($\Delta\alpha$, $\Delta\beta$, and $\Delta\gamma$) are applied in the mirror body frame in Code-V by

$$\Delta\gamma' = 0 \tag{4.14}$$

$$\Delta\beta' = -\Delta\gamma\sin\alpha' + \Delta\beta\cos\alpha' \tag{4.15}$$

$$\Delta\alpha' = \Delta\alpha. \tag{4.16}$$

These transformations are used when applying the rotational perturbations to mirrors with an initial rotational offset.

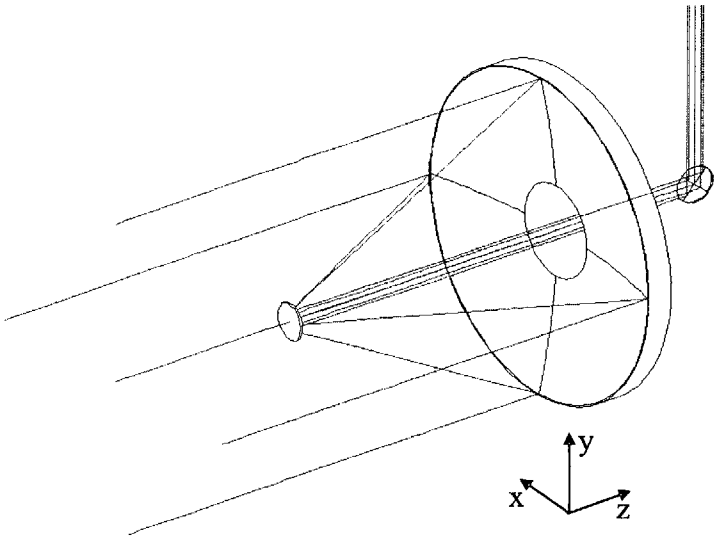

Figure 4-7: Zoomed in view of aperture 1 with CODE-V coordinate frame.

4.5 Hand Calculations

It is good engineering practice to check complex computer models with simple "hand calculations" whenever possible. In this section we check the CODE-V sensitivity results against intuition and simple first-order equations. The equations in this section were derived from original equations developed by Perrygo and Burg [29] for line of sight calculations for JWST (then NGST). These equations were applied to afocal telescopes for interferometry by Chung [5].

The sensitivities listed in this section are straight out of CODE-V before any transformations are applied to convert to the FEM coordinate frame. Figure 4-7 shows a picture of the primary mirror, secondary mirror, and first fold mirror of aperture one. The coordinates in that figure are used in this section.

4.5.1 Pathlength Sensitivity

The CODE-V results for pathlength sensitivity can be verified with intuition alone since they are relatively simple. The aperture one pathlength sensitivity matrix from

CODE-V is:

$$\frac{\delta PL_1}{\delta Q_1} = \begin{bmatrix} 0 & 0 & 2.0 & 0 & 0 & 0 \\ 0 & 0 & -2.0 & 0 & 0 & 0 \\ 0 & -1.0 & 1.0 & 0 & 0 & 0 \\ 0 & 1.0 & -1.0 & 0 & 0 & 0 \\ 0 & 0 & 1.0 & 0 & 0 & 0 \end{bmatrix}. \tag{4.17}$$

The first row lists the pathlength sensitivities to all six degrees of freedom of the primary mirror of aperture one. We see that the only non-zero entry is a sensitivity to motion along the z-axis. Positive motion in the z-direction will move the primary mirror away from the light source and away from the secondary mirror. This will have the effect of increasing the overall pathlength by twice the amount of the z perturbation, since it not only lengthens the light's incoming path but also its outgoing path.

The second row of the matrix corresponds to the pathlength sensitivities to motion of the secondary mirror of aperture one. A motion in the positive z-direction will result in the secondary mirror moving closer to the primary and closer to the first fold mirror. Therefore, the overall optical pathlength will reduce by twice the physical motion in the z-direction.

Rows three and four correspond to the fold mirrors. Moving the first fold mirror in the positive y-direction causes the light to hit the mirror at a point closer to the source. Since the fold mirrors are offset at a 45° angle, there will be a negative one to one ratio. A motion in the positive z-direction will cause a one to one increase in the overall pathlength. The light still hits the center of the fold mirror but the mirror is just farther away now. The second fold mirror has the opposite effect as the first since its light enters along a different axis.

The last row of the matrix represents the image plane. Since the light will be pointed at the center of the image plane, only a motion in the z-axis will cause a change. This change is a one to one ratio.

4.5.2 Wavefront Tilt Sensitivity

Wavefront tilt sensitivities can be verified through the use of simple hand calculations. The CODE-V sensitivity matrix for wavefront tilt about the x-axis in aperture one is:

$$\frac{\delta WTx_1}{\delta Q_1} = \begin{bmatrix} 0 & 0.0079 & 0.0230 & 33.6176 & 0.1736 & 0 \\ 0 & -0.0009 & -0.0122 & -1.8814 & 0.0785 & 0 \\ -0.0017 & -0.0109 & 0.0076 & 2.0419 & -0.0948 & -0.0948 \\ 0.0030 & 0.0124 & -0.0092 & -1.9286 & 0.1733 & 0.1733 \\ 0 & 0 & 0.0098 & 1.0000 & 0 & 0 \end{bmatrix}. \quad (4.18)$$

Changes in wavefront tilt about the x-axis will be caused primarily by rotations of optical elements about their own x-axes. It is these terms, in the fourth column of the matrix in Equation 4.18, that we will want to verify with hand calculations. The other terms are small and can be considered negligible compared to the sensitivities in column four.

A ray reflected by a mirror with a tip or tilt perturbation will have its direction changed by twice the angle of the perturbation. This principal applies to all the mirrors and can be seen in rows two, three and four of column four. The variation in sign is due to the orientation and location of the mirrors. The reason the sensitivity to rotation of the primary mirror (row one) is so much larger is because of a coupling effect with the secondary mirror. The reflected ray from the primary mirror has changed by an angle of twice the perturbation angle. This newly directed ray, however, will strike the secondary mirror at a different location causing an even greater departure from the nominal angle. This effect can be approximated by multiplying by the magnification factor of the telescope, M. Therefore, our wavefront tilt sensitivity to primary mirror rotation about the x-axis estimation equation is:

$$\frac{\delta WTx_1}{\delta Q_1}(1,4)\Big|_{\text{est.}} = 2M \quad (4.19)$$

where

$$M = \frac{-f_1}{f_2} \tag{4.20}$$

and f_1 is the focal length of the primary mirror and f_2 is the focal length of the secondary mirror. We can calculate the focal lengths by using the radius of curvature, R, the conic constant, K, and certain properties of conic sections.

A conic section is defined by its eccentricity, e. The conic section is a circle for $e = 0$, an ellipse for $e < 1$, a parabola for $e = 1$, and a hyperbola for $e > 1$ [16]. The conic constant is related to eccentricity by:

$$K = -e^2. \tag{4.21}$$

Using the values from Table 3.4 and applying Equation 4.21, we find that $e_{primary} = 0.9999982$ and $e_{secondary} = 0.9999696$. Therefore, each mirror is a slightly elliptic conic section revolved around its major axis.

Some properties of an ellipse are shown in Figure 4-8. The major axis length is "2a" and the minor axis length is "2b." We will use the relationships defined in this figure to derive an equation for focal length as a function of R and e. The radius of curvature, R, at the ends of the major axis is

$$R = \frac{b^2}{a}. \tag{4.22}$$

Using the equation

$$b = a\sqrt{1 - e^2}, \tag{4.23}$$

Equation 4.22 reduces to

$$R = a(1 - e^2). \tag{4.24}$$

The focal length, f, is the distance from point "V" to point "F". Looking at Figure 4-8 we see that $f = a - c = a - ea$, or

$$f = a(1 - e). \tag{4.25}$$

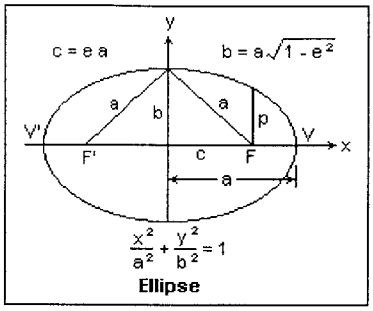

Figure 4-8: Drawing of an ellipse with key properties labelled [18].

Rearranging Equation 4.24 and substituting it into Equation 4.25 we find that

$$f = R\frac{(1-e)}{(1-e^2)}. \tag{4.26}$$

Since our values for e are essentially equal to one, we will want to find the limit of Equation 4.26 as e approaches one. Using L'Hopital's rule:

$$\lim_{e\to 1}\frac{(1-e)}{(1-e^2)} = \lim_{e\to 1}\frac{\frac{d}{de}(1-e)}{\frac{d}{de}(1-e^2)} = \frac{1}{2}. \tag{4.27}$$

Therefore,

$$\lim_{e\to 1} f = \frac{R}{2}. \tag{4.28}$$

Using Equation 4.28, the focal lengths for our nominal design are $f_1 = 3.5$ m and $f_2 = -0.20381$ m. Plugging these values into Equation 4.20 gives us a magnification factor of $M = 17.17$. Therefore, our estimated wavefront tilt sensitivity to primary mirror rotation, from Equation 4.19 is $2 * 17.17 = 34.34$. This is reasonably close to our CODE-V generated value of 33.62.

4.5.3 Beam Shear Sensitivity

The beam shear sensitivity matrices for both the x and y direction of aperture one are:

$$\frac{\delta BSx_1}{\delta Q_1} = \begin{bmatrix} 125.0600 & 0 & 0 & 0 & -875.3924 & 0 \\ -124.1100 & 0 & 0 & 0 & 50.5922 & 0 \\ 0 & 0 & 0 & 0 & -20.2965 & -20.2965 \\ 0 & 0 & 0 & 0 & 0.2962 & 0.2962 \\ -1.0000 & 0 & 0 & 0 & 0 & 0 \end{bmatrix} \tag{4.29}$$

$$\frac{\delta BSy_1}{\delta Q_1} = \begin{bmatrix} 0 & 125.0600 & 0 & 875.3695 & 0 & 0 \\ 0 & -124.1100 & 0 & -50.5922 & 0 & 0 \\ 0 & -1.0000 & 1.0000 & 40.5923 & 0 & 0 \\ 0 & 1.0000 & -1.0000 & -0.5924 & 0 & 0 \\ 0 & -1.0000 & 0 & 0 & 0 & 0 \end{bmatrix}. \tag{4.30}$$

Since very small perturbations are being used, the small angle approximation applies. This approximation states that for small angles, θ,

$$\sin(\theta) = \theta \tag{4.31}$$

and

$$\cos(\theta) = 1. \tag{4.32}$$

Therefore, if θ is the change in trajectory of a ray of light, the change in location of the point where the ray strikes the next mirror will be

$$\Delta d = L\theta \tag{4.33}$$

where L is the distance to the next mirror. We will use these principals to hand calculate the beam shear sensitivities and verify our CODE-V results. First we will look at the primary mirror. We know from before that if the primary is given a tilt perturbation of $\Delta\theta_x$ the reflected ray will have a change in angle of $2\Delta\theta_x$. This ray

will hit the secondary mirror at a change in location along the y-axis of Δy_{sec}, where

$$\Delta y_{sec} = 2\Delta\theta_x \overline{PS} \tag{4.34}$$

and $\overline{PS}$ is the distance from the primary to the secondary mirror. Because the ray hits the secondary in a new location, the reflected ray will change its angle again and have a new trajectory of $2M\Delta\theta_x$. Since the rest of the mirrors along the optics train are fold mirrors we can jump ahead and calculate the total beam shear at the image plane (the fold mirror redirections can be neglected for the beam shear calculation as long as they have no perturbations). The total image plane beam shear is

$$\Delta y_{im} = 2\Delta\theta_x \overline{PS} + 2\Delta\theta_x M\overline{SI} \tag{4.35}$$

where $\overline{SI}$ is the distance from the secondary mirror to the image plane. The partial derivative is found by dividing by $\Delta\theta_x$:

$$\frac{\delta BS_{y_1}}{\delta Q_1}(1,4)\bigg|_{est.} = \frac{\Delta y_{im}}{\Delta\theta_x} = 2\overline{PS} + 2M\overline{SI}. \tag{4.36}$$

In our design, $\overline{PS} = 3.296186$ m and $\overline{SI} = 25.296186$ m. This gives us a sensitivity of $\frac{\Delta y_{im}}{\Delta\theta_x} = 875.2634$. This is almost exactly the same as our CODE-V derived value so we can feel confident about our results.

Next, we hand calculate beam shear sensitivity to a primary mirror translational perturbation. The equation defining this sensitivity is:

$$\frac{\delta BS_{y_1}}{\delta Q_1}(1,2)\bigg|_{est.} = \frac{1}{2}\frac{1}{f_1}(\overline{PS} + M\overline{SI}). \tag{4.37}$$

Substituting the proper values into Equation 4.37 we find that the hand calculation gives us a value of 124.6. This verifies the CODE-V generated value of 125.06.

Similar calculations can be performed to verify the rest of the sensitivity values. By verifying these sensitivity results with hand calculations and intuition, we gain a level of confidence in our optical modeling technique. Now we can move into the final

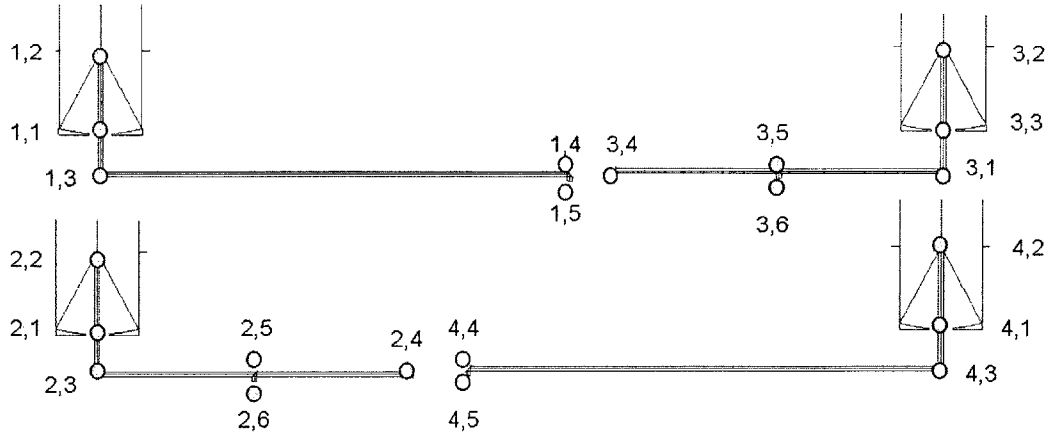

Figure 4-9: Ray trace for each aperture depicting all mirrors.

section where the full sensitivity matrix is assembled.

4.6 The Optical Sensitivity Matrix

The final step in generating performance outputs is to map the locations of the mirrors in the optical model to a set of critical nodes in the finite element model. Figure 4-9 depicts the ray trace of each aperture of the interferometer as it is modeled in Code-V. Each mirror is labelled with an (i, j) index. The value i corresponds to the aperture number. The value j is the mirror number corresponding to its place in order in its aperture's optics train. These labels are also shown on the FEM in Figure 4-10 near a dot representing their corresponding critical node. There is a critical node at the center of each primary and secondary mirror as well as at the location of the combiner. Sensitivities are added for critical nodes representing multiple mirrors. Therefore, using the mapping technique displayed in Figure 4-10 and with aperture $i = 1$, Equation 4.1 will reduce to

$$\Delta PL_1 = \left(\frac{\delta P_{1,1}}{\delta Q_{1,1}} + \frac{\delta P_{1,3}}{\delta Q_{1,3}}\right) Q_{1,1} + \frac{\delta P_{1,2}}{\delta Q_{1,2}} Q_{1,2} + \left(\frac{\delta P_{1,4}}{\delta Q_{1,4}} + \frac{\delta P_{1,5}}{\delta Q_{1,5}}\right) Q_C \qquad (4.38)$$

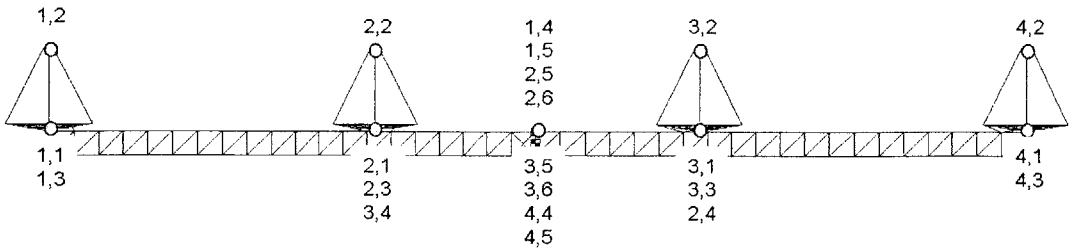

Figure 4-10: Critical Nodes in FEM that utilize sensitivities of one or more mirrors from Code-V model.

where Q_C contains the degrees of freedom of the combiner node. Equations 4.4 and 4.6 will reduce in similar fashion.

As explained before, OPD is the difference in pathlength between two apertures. The differences between apertures one and two, one and three, and one and four are calculated by the following equations:

$$OPD_{12} = \Delta PL_1 - \Delta PL_2 \tag{4.39}$$

$$OPD_{13} = \Delta PL_1 - \Delta PL_3 \tag{4.40}$$

$$OPD_{14} = \Delta PL_1 - \Delta PL_4. \tag{4.41}$$

All other OPD combinations can be derived from the results of the equations above.

Likewise, Differential Wavefront Tilt is found by finding the relative difference in wavefront tilt of two apertures. The wavefront tilt is measured about two axes resulting in a total of six equations:

$$DWT_{x_{12}} = \Delta WT_{x_1} - \Delta WT_{x_2} \tag{4.42}$$

$$DWT_{y_{12}} = \Delta WT_{y_1} - \Delta WT_{y_2} \tag{4.43}$$

$$DWT_{x_{13}} = \Delta WT_{x_1} - \Delta WT_{x_3} \tag{4.44}$$

$$DWT_{y_{13}} = \Delta WT_{y_1} - \Delta WT_{y_3} \tag{4.45}$$

$$DWT_{x_{14}} = \Delta WT_{x_1} - \Delta WT_{x_4} \tag{4.46}$$

$$DWT_{y_{14}} = \Delta WT_{y_1} - \Delta WT_{y_4}. \tag{4.47}$$

Finally, Differential Beam Shear is found by finding the relative difference in beam shear between two apertures. Differential Beam Shear is also measured along two axes resulting in a total of six equations:

$$DBS_{x_{12}} = \Delta BS_{x_1} - \Delta BS_{x_2} \tag{4.48}$$

$$DBS_{y_{12}} = \Delta BS_{y_1} - \Delta BS_{y_2} \tag{4.49}$$

$$DBS_{x_{13}} = \Delta BS_{x_1} - \Delta BS_{x_3} \tag{4.50}$$

$$DBS_{y_{13}} = \Delta BS_{y_1} - \Delta BS_{y_3} \tag{4.51}$$

$$DBS_{x_{14}} = \Delta BS_{x_1} - \Delta BS_{x_4} \tag{4.52}$$

$$DBS_{y_{14}} = \Delta BS_{y_1} - \Delta BS_{y_4}. \tag{4.53}$$

The coefficients of Equations 4.39 through 4.53 populate the 15x54 C matrix of the state-space output equation from Chapter 2:

$$y = C\hat{x}, \tag{4.54}$$

where the states of interest are:

$$\hat{x} = \begin{pmatrix} Q_C & Q_{1,1} & Q_{1,2} & Q_{2,1} & Q_{2,2} & Q_{3,1} & Q_{3,2} & Q_{4,1} & Q_{4,2} \end{pmatrix}^T. \tag{4.55}$$

Keeping in line with the derivation in Chapter 2, Equation 4.56 is applied in modal form by

$$y = C\Phi\hat{q} \tag{4.56}$$

excluding velocity states.

Now that we have the C matrix, we can run the frequency domain disturbance analysis and find the RMS performance outputs for this model.

Chapter 5

Disturbance Model

In order to accurately predict the performance of a high precision optical spacecraft, relevant disturbance sources must be modeled. Disturbances can come from external sources such as gravity gradients and solar pressure. It may also result from internal sources such as reaction wheels, cryocoolers, servomechanisms and sensor noise. We choose to model two forms of disturbances in this analysis. First, we model static and dynamic imbalances in the reaction wheels since they are the largest disturbance source on most spacecraft. These disturbances are inputs to the plant and apply forces and torques about all six degrees of freedom. Secondly, we model sensor noise since it will likely be a driving factor in meeting the null stability requirement. This disturbance is added to the outputs of the optical sensitivity matrix and degrades the inputs to the optical controllers. Figure 5-1 highlights the areas of the model that will be discussed in this chapter.

5.1 Reaction Wheel Disturbances

Reaction wheel imbalance is the largest source of disturbances for most spacecraft. As such, it is very important to understand the effects of these disturbances on spacecraft performance. Much work has been done on modeling reaction wheel disturbances in recent years. Melody developed a stochastic broadband modeling method for reaction wheel disturbances [26]. His work focused on the Hubble Space Telescope wheels but

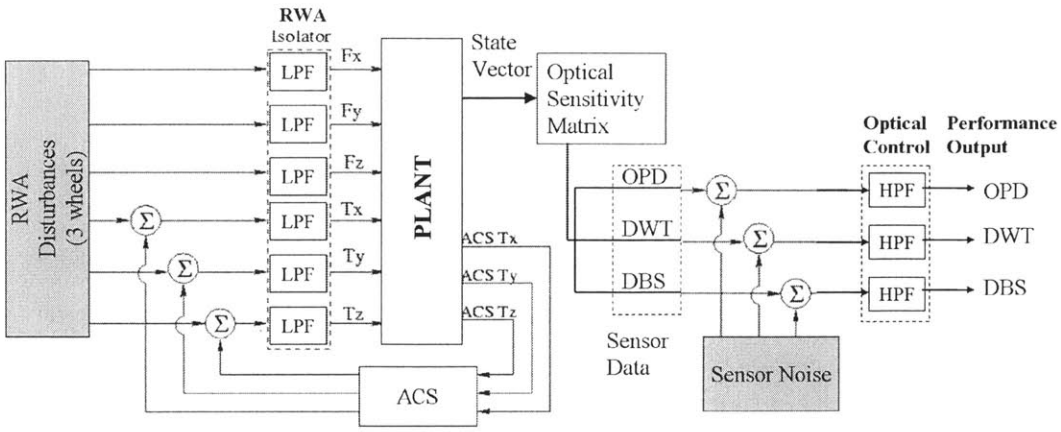

Figure 5-1: Integrated model block diagram with disturbance sources highlighted

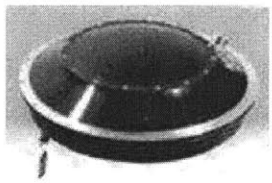

Figure 5-2: Ithaco E-type reaction wheel [23]

the method is applicable to all wheels. Masterson used Melody's method to develop models of the Ithaco B-type and Ithaco E-type wheels [23].

For our analysis, we will use Masterson's power spectral density disturbance model of the Ithaco E-type wheel. The Ithaco wheel used to generate this model was an off-the shelf product that had not been balanced for "minimum vibration operation" [23]. Figure 5-2 shows a picture of the E-type wheel. Three of these wheels are used and placed at the center of the spacecraft truss in an orientation explained in Figure 5-3. Using the experimental data of the Ithaco E-type wheel, disturbance PSDs are generated for all six degrees of freedom (3 forces and 3 moments). Figure 5-4 shows the disturbance spectrum for one of these degrees of freedom. Data is generated for wheels operating from 0-3000 RPM with a frequency range of 0-278 Hz.

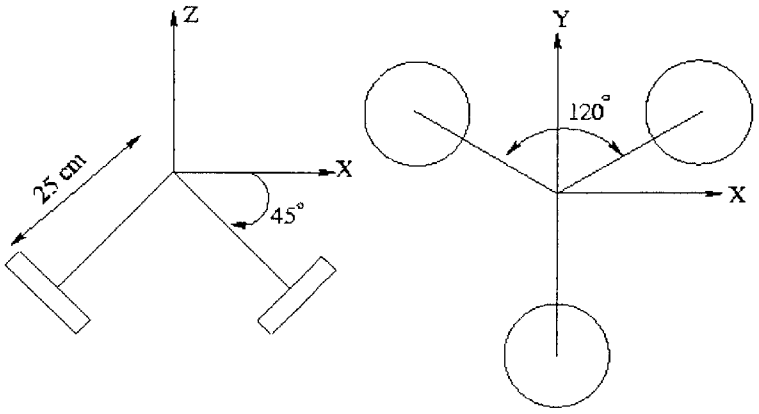

Figure 5-3: Reaction wheel assembly orientation

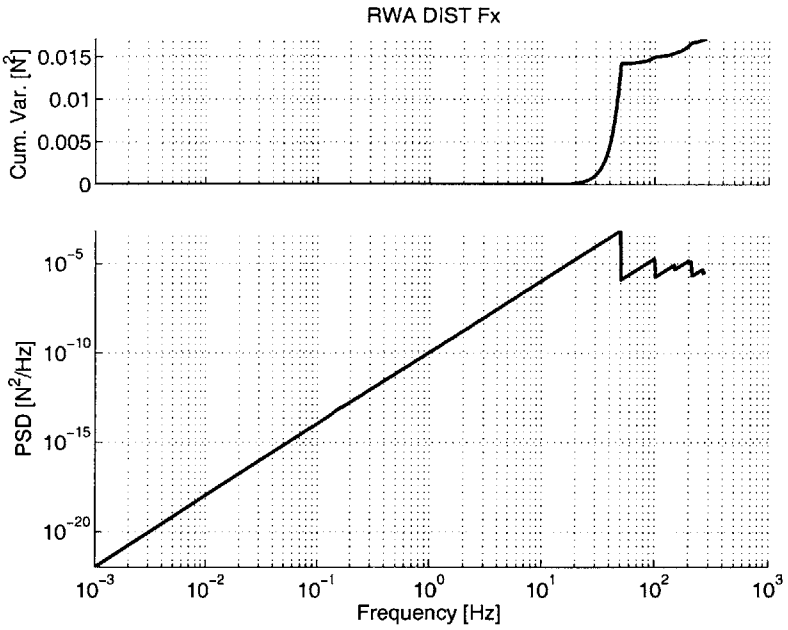

Figure 5-4: Reaction wheel disturbance spectrum for x-axis forcing

5.2 Sensor Noise

In order to achieve optical requirements, a set of controllers will be used to minimize OPD, DWT, and DBS. This control capability will likely be implemented with fast steering mirrors (FSMs) and optical delay lines (ODLs). A suite of sensors will measure the optical error and provide inputs to the controller. However, perfect measurements cannot be made due to sensor noise. One example is fine guidance sensor error arising from photon noise [8]. Contributing factors to this error include detector quantum efficiency, integration time and guide star magnitude [8]. Precise sensor models for TPF, however, are not available at this time. Therefore, as a start, we model sensor noise as providing an RMS error equal to half the requirement for OPD, DWT, and DBS.

Sensor noise is modeled as a low-pass shaping filter with a white noise input. This is done so that a PSD can be generated and used in our frequency domain analysis. The transfer function of the low-pass filter, $G_{LP}(s)$, takes the form

$$G_{LP}(s) = \frac{bc}{s-a} \tag{5.1}$$

where bc is the gain, a is the cutoff frequency, and a, b, and c are 1×1 matrices in the state-space equations.

By driving this filter with a PSD input $S_{uu}(s)$, the output PSD is found by evaluating the expression

$$S_{xx}(s) = G_{LP}(s)S_{uu}(s)G_{LP}(s)^H \tag{5.2}$$

where $G_{LP}(s)^H$ is the complex conjugate transpose of $G_{LP}(s)$. For a unity white noise input, $S_{uu}(s) = 1$, Equation 5.2 reduces to

$$S_{xx}(s) = G_{LP}(s)G_{LP}(s)^H. \tag{5.3}$$

The mean square value of the output is given by

$$E[x^2] = \frac{1}{2\pi j}\int_{-j\infty}^{j\infty} S_{xx}(s)ds. \tag{5.4}$$

In order to solve this equation by use of an integral table, we must first factor $S_{xx}(s)$:

$$S_{xx}(s) = \frac{h(s)}{d(s)}\frac{h(-s)}{d(-s)} \tag{5.5}$$

where

$$G_{LP}(s) = \frac{h(s)}{d(s)}. \tag{5.6}$$

Now we can solve Equation 5.4 by using the integral table from Brown and Hwang [3]:

$$I_n = \frac{1}{2\pi j}\int_{-j\infty}^{j\infty}\frac{h(s)}{d(s)}\frac{h(-s)}{d(-s)}ds \tag{5.7}$$

$$h(s) = h_{n-1}s^{n-1} + h_{n-2}s^{n-2} + \ldots + h_0 \tag{5.8}$$

$$d(s) = d_n s^n + d_{n-1}s^{n-1} + \ldots + d_0 \tag{5.9}$$

$$I_1 = \frac{h_0^2}{2d_0d_1}. \tag{5.10}$$

Requirements on each performance metric are given as RMS (root mean square) values. The integral table solves for mean square value which is just RMS squared. In G_{LP}, the values for a and b are set equal to the bandwidth of the optical controller, f_{oc}. Therefore, we want to find the value of c that will give us a mean square value output equal to the RMS requirement squared.

Setting a and b equal to f_{oc}, equation 5.1 becomes

$$G_{LP}(s) = \frac{f_{oc}c}{s - f_{oc}}. \tag{5.11}$$

Setting the numerator of equation 5.11 equal to $h(s)$ in equation 5.8 and the denominator equal to $d(s)$ in equation 5.9 we find that $h_0 = f_{oc}c$, $d_0 = f_{oc}$ and $d_1 = 1$. Using these values and setting $I_1 = req^2$, equation 5.10 becomes

$$req^2 = \frac{f_{oc}c^2}{2}. \tag{5.12}$$

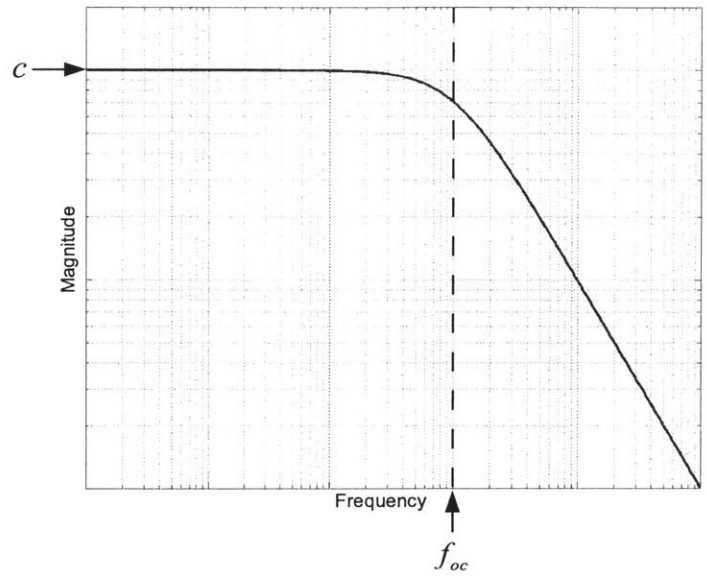

Figure 5-5: Sensor noise shaping filter.

Rearranging equation 5.12 we find that

$$c = \sqrt{\frac{2req^2}{f_{oc}}} \tag{5.13}$$

We now have the values for a, b and c and can create the proper low-pass shaping filter to simulate sensor noise. The filter is shown in Figure 5-5. The axis labels and values in the figure are intentionally left blank since they will be defined by the optical control bandwidth and the performance requirement. The cutoff frequency is defined by f_{oc} and the gain is the value c. The filter is implemented in state-space form and its outputs are added to the outputs of the optical sensitivity matrix.

Chapter 6

Disturbance Rejection

The primary source of disturbances for TPF will likely be caused by the imbalance of the rotating reaction wheels. If the vibrations from this disturbance are not properly attenuated, the optical performance requirements will never be met. One mitigation strategy is to use a combination of high frequency attenuation at the disturbance input and low frequency attenuation at the performance output [28]. As shown in Figure 6-1, this chapter will cover the reaction wheel isolation system, the optical control system and the attitude control system (ACS).

6.1 Reaction Wheel Vibration Isolation System

In practice, the job of high frequency disturbance attenuation will be done by a combination of passive and active vibration isolation. The idea is to allow the low frequency torques to be passed into the spacecraft bus to perform the attitude adjustments while blocking out the high frequency disturbances that will degrade optical performance. Figure 6-2 shows a picture of a six-axis "hexapod" active reaction wheel assembly (RWA) vibration isolator built by JPL. Each strut of the hexapod contains a diaphragm, which acts as a soft spring, as well as a voice coil actuator. The diaphragm acts as the passive isolator while the voice coil performs active vibration isolation through feedback control [28].

For early design trades such as our TPF analysis, we can model the RWA isolator

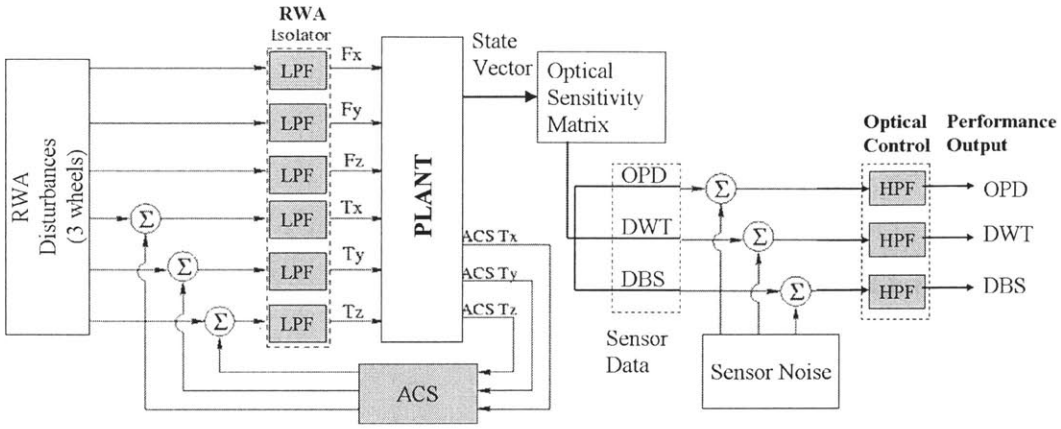

Figure 6-1: Integrated model block diagram with disturbance rejection/control elements highlighted

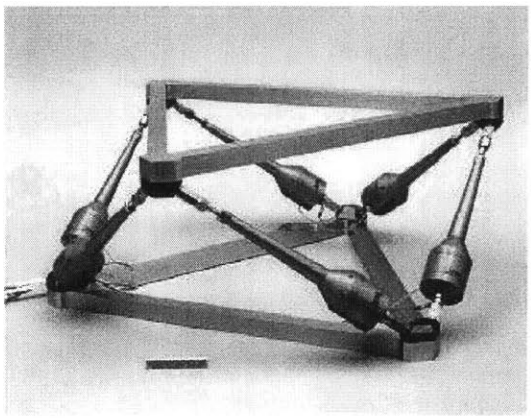

Figure 6-2: JPL hexapod isolator [30]

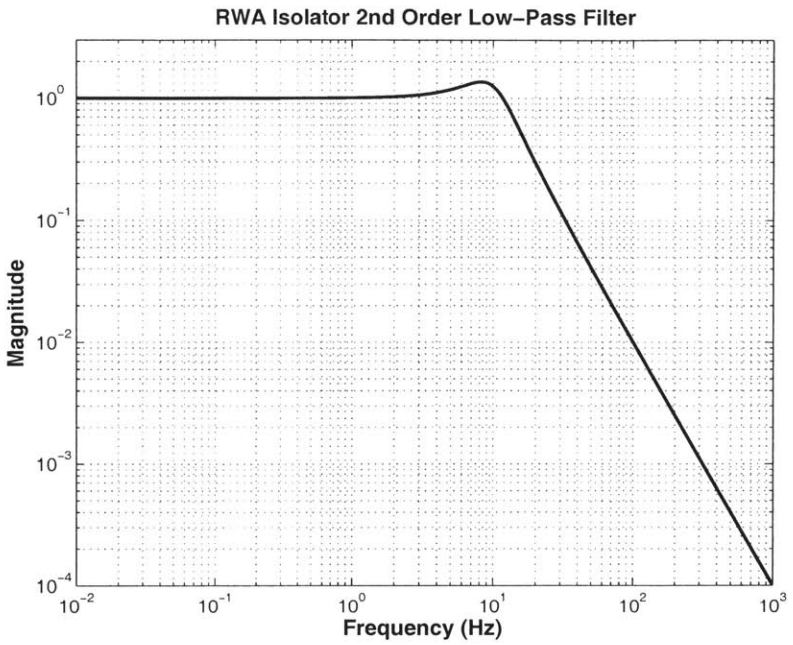

Figure 6-3: Reaction wheel assembly isolator modeled as second order low pass filter. Nominal cutoff freq=10 Hz, Nominal damping ratio=0.4.

as a second order low pass filter as shown in Figure 6-3. The transfer function for this filter is

$$G_{iso} = \frac{(2\pi f_{iso})^2}{s^2 + 2\zeta_{iso}(2\pi f_{iso})s + (2\pi f_{iso})^2} \tag{6.1}$$

where f_{iso} is the cutoff frequency and ζ_{iso} is the damping ratio. The nominal values are $f_{iso} = 10\text{Hz}$ and $\zeta_{iso} = 0.4$.

The proper relationship between RWA isolator cutoff frequency and optical control bandwidth must be found so that the two attenuation methods compliment one another while minimizing the disturbance leakage. We therefore set the cutoff frequency to be a DOCS perturbable design parameter so that optimizations may be performed later.

6.2 Optical Control System

Low frequency attenuation is performed by active optical controllers located along the optical train. In practice, actuators such as fast steering mirrors (FSMs) and optical delay lines (ODLs) will be used for the optical control. Figure 6-4 shows an example of an FSM. The FSM can tip and tilt to alter the wavefront tilt of the incoming beam of light. ODLs work by piston movement to change the overall pathlength of the light beam.

In order to simplify our analysis, the effects of the optical controllers are modeled as first order high pass filters. The transfer function for the optical control filter is

$$G_{oc}(s) = \frac{s}{s + (2\pi f_{oc})} \tag{6.2}$$

where the nominal cutoff frequency, f_{oc}, is 100 Hz. This transfer function is plotted in Figure 6-5. We want the control bandwidth to be high enough to attenuate enough of the performance errors to meet the requirements. The main limiting factor on bandwidth is computational cost. Therefore, the control bandwidth is also set as a DOCS perturbable design parameter so that trade studies and design optimizations can be performed.

As described in Chapter 5, sensor noise is added to the performance outputs of the integrated model before they are sent through the optical control filter. The final performance values for OPD, DWT and DBS come from the output of the optical controller.

6.3 Attitude Control System

An attitude control system (ACS) will provide the pointing stability for TPF. Rotational rigid body modes are contained in the structural model that, without the use of an ACS, will hinder the optical performance. The ACS is modeled as a proportional-derivative controller using a predefined DOCS function. The control bandwidth is set to 0.01 times the first mode frequency of the plant. This is done to prevent interaction

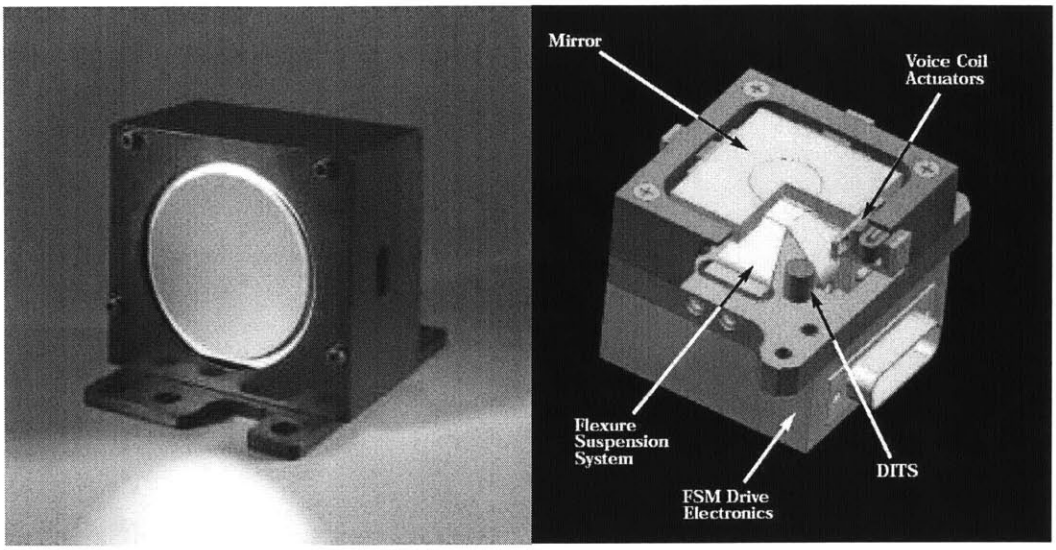

Figure 6-4: Fast steering mirror example (by Newport) [6]

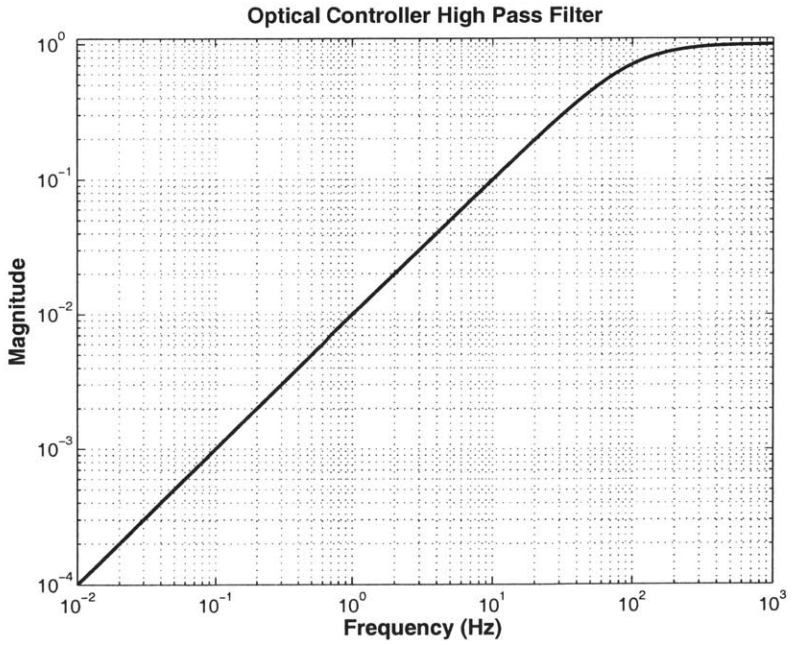

Figure 6-5: Optical controller high pass filter. Nominal cutoff freq=100Hz

between the controller and the flexible modes of the structure. The bandwidth can be altered by changing the appropriate value within `DesignVector`.

Chapter 7

Optical Performance Analysis

In this chapter we link together the different individual models to create the full integrated model. The disturbance analysis is then performed and RMS optical performance outputs are calculated. Using the DOCS toolbox, we make certain design parameters perturbable. This allows us to determine how to improve performance without having to regenerate the FEM over and over again.

7.1 Nominal Performance

First we will look at the nominal performance of the integrated model. The three main performance metrics are Optical Pathlength Difference (OPD), Differential Wavefront Tilt (DWT) and Differential Beam Shear (DBS). In addition to these performance metrics, we extract spacecraft mass, mode shapes and frequencies. These are also important characteristics to keep in mind when designing a spacecraft.

The first six modes of the FEM are all rigid body modes with frequencies nearly equal to zero. Table 7.1 lists the first six flexible modes (modes 7-12) along with the corresponding frequencies and a description of the mode shapes. Pictures of three of the mode shapes, generated by the post-processing software FEMAP®, are depicted in Figure 7-1. The spacecraft mass breakdown is listed in Table 7.2.

Different components of the integrated model can be used as desired. For example, one may want to create an integrated model with and without the RWA isolator

Table 7.1: First six non-rigid body modes

Mode No.	Frequency (Hz)	Description
7	1.2121	1^{st} bending about y-axis
8	1.243	1^{st} bending about z-axis
9	3.3983	2^{nd} bending about z-axis with mirror tilt
10	3.744	2^{nd} bending about y-axis
11	3.7939	Torsion mode. Apertures 1&2 in phase, 3&4 in phase
12	4.437	Torsion mode. Apertures 1&4 in phase, 2&3 in phase

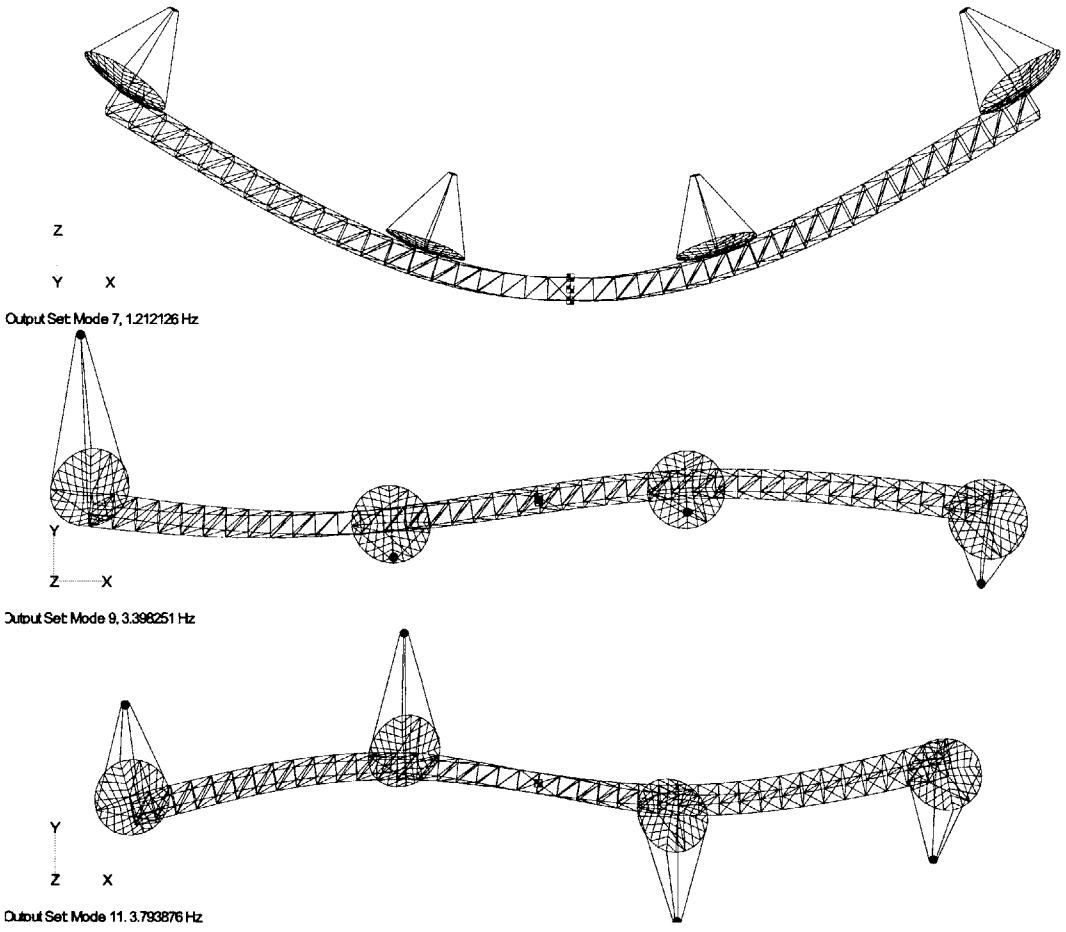

Figure 7-1: Selected mode shapes

Table 7.2: TPF mass breakdown.

Component	Mass (kg)
Truss	585
Bus	520
Combiner	430
RWA	32
Collectors	639
Total	**2206**

to observe its effect on performance. Twelve integrated model combinations are outlined in Table 7.3. The table shows the name of each integrated model and has a star underneath each component it contains. Table 7.4 shows three of the performance outputs for each integrated model and the nominal requirement for each performance metric. We can see that the addition of optical control and RWA isolators dramatically improves the optical performance. The attitude control system has little to no effect on the performance. Sensor noise degrades the performance slightly. The amount of performance degradation is dependent on the value used in the sensor noise model. The sensor noise is set to one half of requirement value for each performance metric from Table 4.1.

The lack of effect on performance by the ACS is an area of concern that is investigated by looking at the integrated model transfer functions. Figure 7-2 shows magnitude and phase plots for the transfer functions of OPD13 over RWA disturbance torque about the y-axis. The plot on the right includes the use of ACS while the plot on the left does not. In the left plot we see that there is a constant negative slope at very small frequency values. This indicates the presence of a rigid body mode near zero frequency. In the plot on the right we see that the rigid body mode is attenuated by the ACS. The bandwidth of the ACS, as defined in Chapter 6, is set at 0.01 times the first mode frequency. This is verified in the graph as the first structural mode is slightly above 1 Hz and the knee in the ACS portion is near 0.01 Hz. The ACS is set at this low frequency to prevent interaction with the flexible structural modes.

It is important to note the change in the transfer function in Figure 7-2 indicates that the ACS is doing its job. The reason we do not see much of a change in RMS

output is due to the shape of the RWA disturbance PSD. Recall that the RMS is found by integrating the output PSD and taking its square root. The output PSD, $S_{xx}(s)$, due to input PSD, $S_{uu}(s)$ is found by

$$S_{xx}(s) = G(s)S_{uu}G_{uu}^{H} \tag{7.1}$$

where $G(s)$ is the system transfer function. Figure 7-3 shows the RWA disturbance input PSD for torque about the y-axis. The power in the low frequency ranges, where the ACS has its effect, is nearly zero. Therefore, when calculating the output PSD, virtually no change will be found between the ACS and non-ACS versions. Figure 7-4 shows that these output PSDs, and their cumulative variances, almost perfectly overlap. If a disturbance source with more energy at low frequencies (such as white noise) were used, we would likely see a more significant change in PSD output with the addition of the ACS.

Cumulative variance plots, like the one in Figure 7-4, essentially give us a running total of the integral that calculates mean square value. This allows us to see which modes in the system cause the most performance degradation. By examining this plot we see that there is a large jump in variance at a mode around 20 Hz. Once modes like this are identified, we can determine if strategies should be employed to prevent disturbances in the problematic region. For example, designers might decide that reaction wheels should not spin in certain speed ranges while optical observations are taking place.

7.2 Parameter Variation

As seen in Table 7.4, our full integrated model comes close but does not meet the performance requirements. Redesign will be necessary if TPF is to achieve its observational goals. Two methods of parameter variation are used to determine redesign options. The first method involves changing the values in `DesignVector` and regenerating the entire integrated model. This method is computationally intensive and

Table 7.3: Integrated model combinations

Model Name	RWA Isolator	ACS	Sensor Noise	Optical Control
OL				
CL_ACS		*		
CL_OC				*
CL_SN_OC			*	*
CL_ACS_OC		*		*
CL_ACS_SN_OC		*	*	*
OL_ISO	*			
CL_ISO_ACS	*	*		
CL_ISO_OC	*			*
CL_ISO_SN_OC	*		*	*
CL_ISO_ACS_OC	*	*		*
CL_ISO_ACS_SN_OC	*	*	*	*

Table 7.4: Nominal RMS values of OPD, DWT and DBS for each integrated model

Model Name	OPD12 (nm)	DWTx12 (nrad)	DBSx12 (μm)
OL	62.14	1090	62.47
CL_ACS	62.16	1090	62.48
CL_OC	12.28	203	17.25
CL_SN_OC	12.31	204	17.25
CL_ACS_OC	12.28	203	17.25
CL_ACS_SN_OC	12.31	204	17.26
OL_ISO	53.04	909	14.01
CL_ISO_ACS	53.08	909	14.01
CL_ISO_OC	4.22	94	2.84
CL_ISO_SN_OC	4.29	97	2.87
CL_ISO_ACS_OC	4.22	94	2.84
CL_ISO_ACS_SN_OC	4.29	97	2.87
Requirement	1.01	50.81	1.59

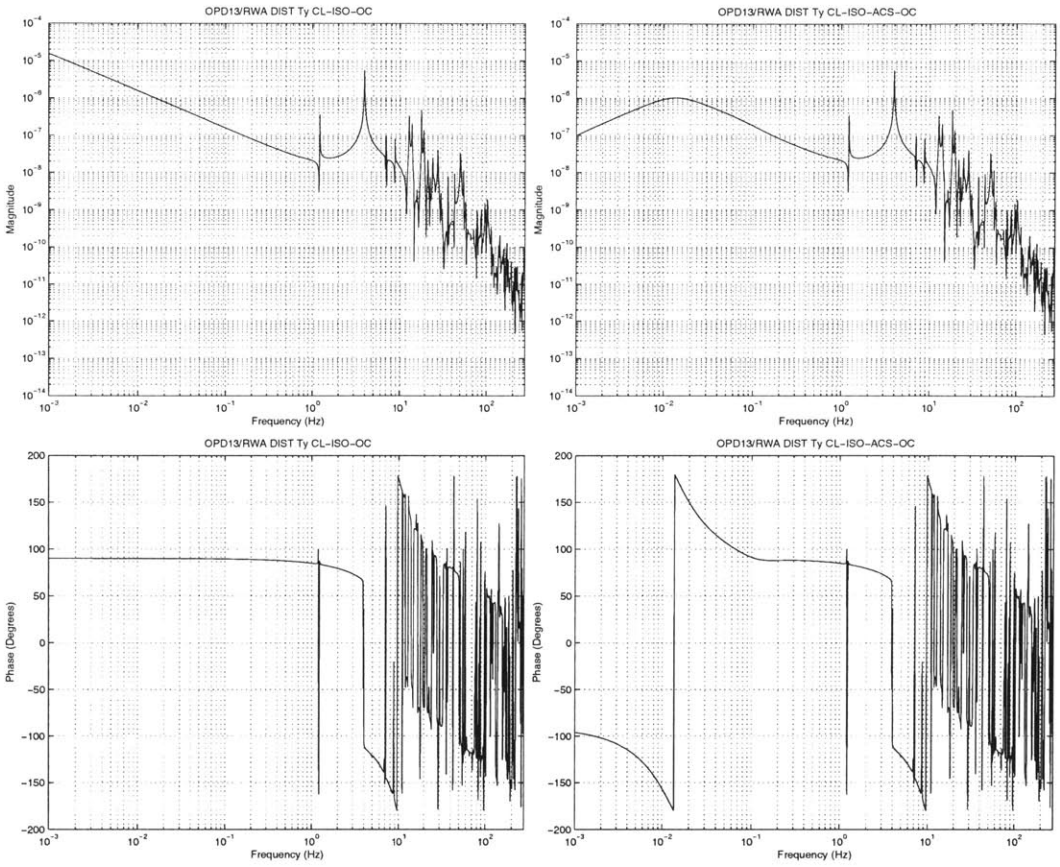

Figure 7-2: Transfer functions of OPD13 over RWA disturbance Ty without ACS (left) and with ACS (right).

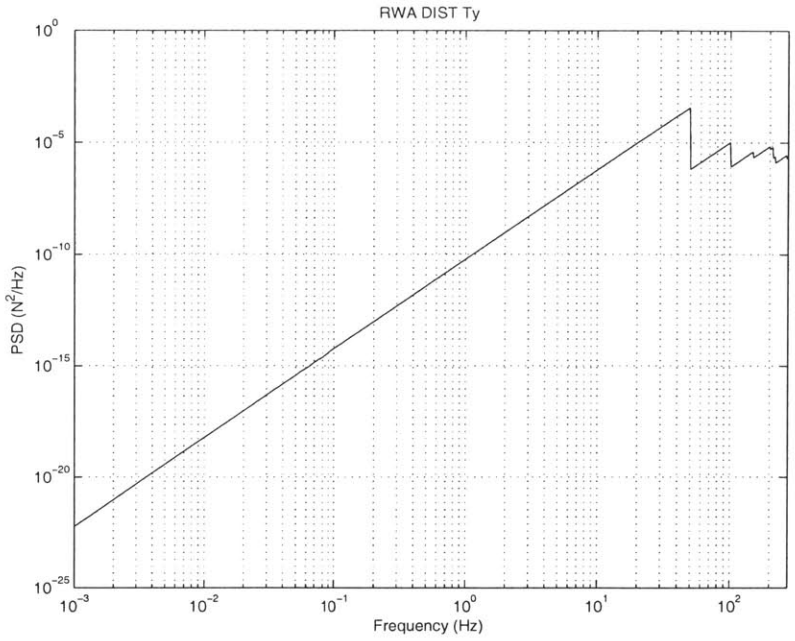

Figure 7-3: Reaction wheel disturbance PSD (torque about y-axis)

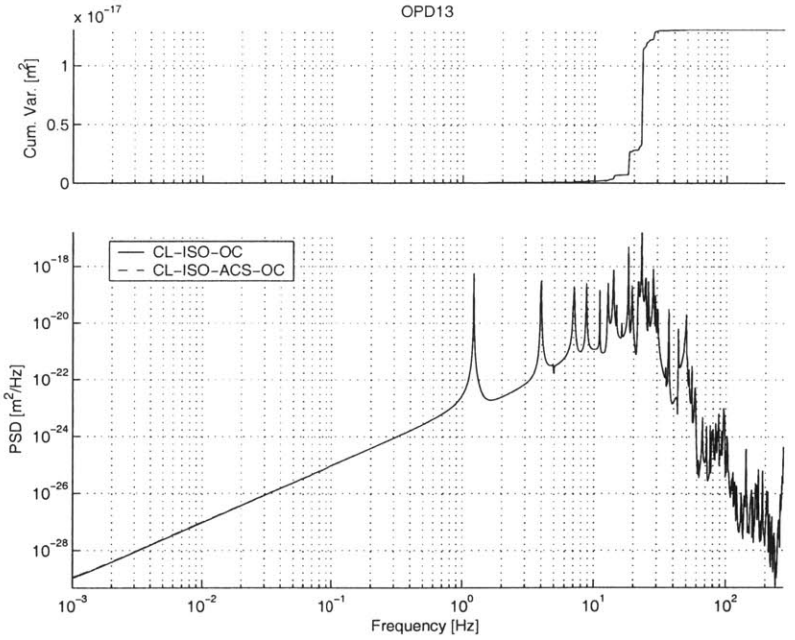

Figure 7-4: Cumulative variance PSD plot of OPD13 with and without ACS

therefore very slow for performing design trades. This method must be used, however, for variations in structure geometry. The second method utilizes the DOCS system's ability to designate perturbable parameters during model generation. Performance sensitivities to the specified parameters are calculated so that quick design trades can be performed after the model is fully generated.

7.2.1 DOCS Perturbations

Since the DOCS perturbation method is more conducive to design trades, we will explore this area first. Any number of design variables can be set as DOCS perturbable parameters. For this analysis we will look at RWA isolator cutoff frequency and optical control bandwidth. Recall that the RWA isolators are modeled as second order low pass filters and the optical controllers are modeled as first order high pass filters. The RWA isolator cutoff frequency is the frequency where the magnitude is 3 db below the DC gain. Likewise, the optical control bandwidth is the frequency where the magnitude of the filter is 3 db below the DC gain.

RWA Isolator Cutoff Frequency

The nominal RWA isolator cutoff frequency is 10 Hz. We will vary this cutoff frequency from 1 Hz to 25 Hz, effectively sliding the filter left and right. Figure 7-5 shows OPD as a function of RWA isolator cutoff frequency. By lowering the cutoff frequency, the low pass filter attenuates more and more of the high frequency disturbance from the reaction wheels. This results in smaller OPD and improved performance. Based on this data alone, one would deduce that the cutoff frequency should be made as small as possible.

The tradeoff that is not depicted in Figure 7-5 is the adverse effects on control authority as RWA isolator cutoff frequency is reduced. As described in Chapter 6, the RWA isolator can be thought of as a spring-damper system. When cutoff frequency is reduced, this spring will get softer. As cutoff frequency approaches zero, the spring will effectively disappear and none of the torques for attitude control will

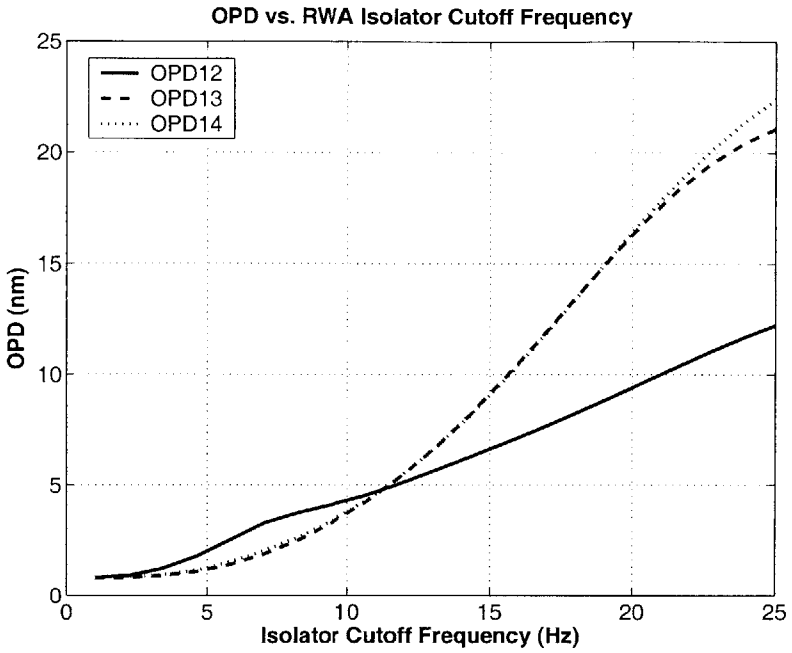

Figure 7-5: OPD as a function of RWA isolator cutoff frequency

be transferred to the structure. Therefore, one must set a minimum cutoff frequency based on the required low-frequency control authority.

Figure 7-6 shows the effects of RWA isolator cutoff frequency on the other performance metrics of DWT and DBS. The plots in this figure show similar trends to that of the OPD figure. We can use these figures to determine what RWA isolator cutoff frequency will allow us to meet our nominal performance requirements. As mentioned in Chapter 4, the requirements for TPF have not been fully determined yet. Therefore, these plots are intended to demonstrate the method for finding improved designs and to show general trends rather than to make specific design recommendations.

Optical Control Bandwidth

Using the same method described in the previous section with the RWA isolator, we can vary optical control bandwidth and find the effects on performance. The nominal optical control bandwidth is 100 Hz. This parameter will be varied from 10 Hz to 200 Hz. Figures 7-7 and 7-8 show the effects of optical control bandwidth on OPD, DWT

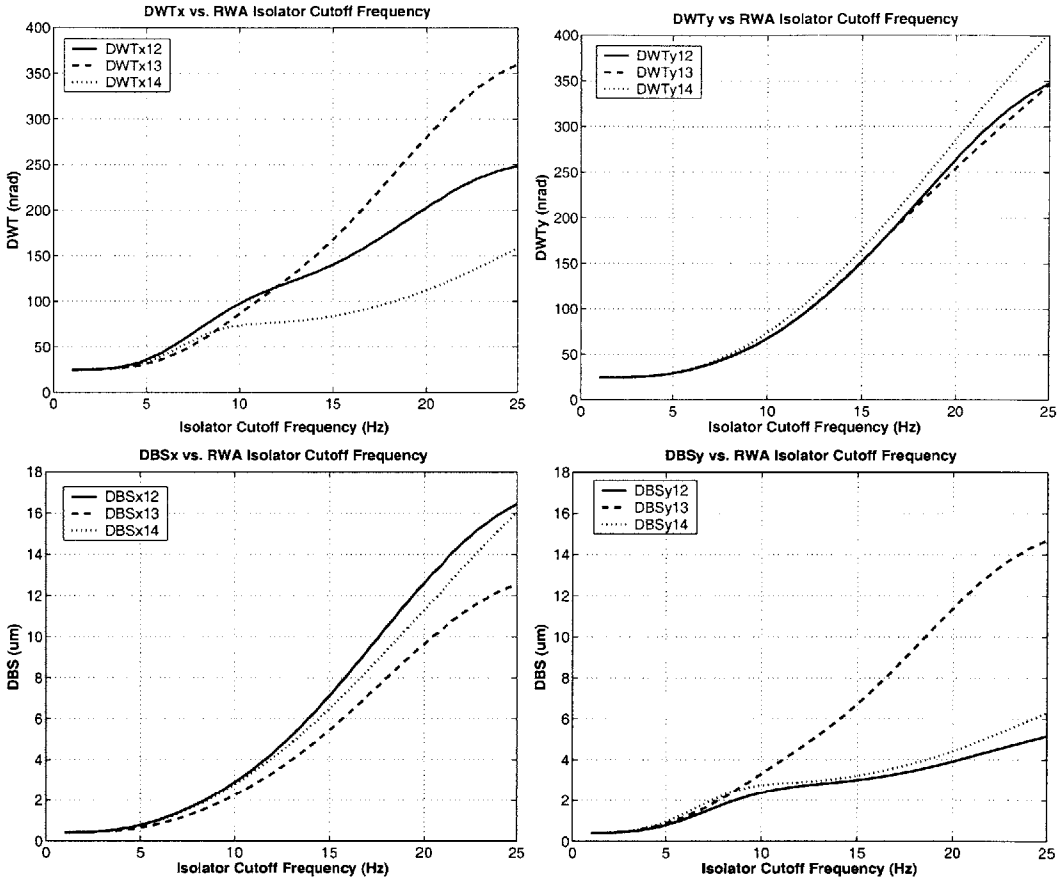

Figure 7-6: DWT and DBS as a function of RWA isolator cutoff frequency

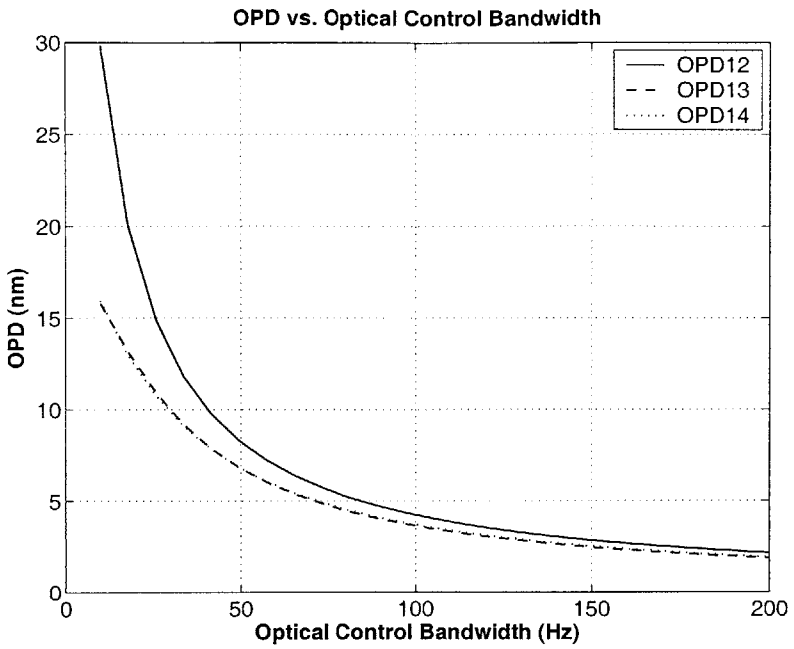

Figure 7-7: OPD as a function of Optical Control Bandwidth

and DBS. At first glance these plots tell us to make the optical control bandwidth as high as possible to improve performance. There are, however, constraining tradeoffs on increasing control bandwidth such as computation costs and sensor limitations.

Isoperformance Contours

It is also possible to vary both RWA isolator cutoff frequency and optical control bandwidth to determine combined performance enhancement strategies. The contour plots in Figures 7-9 and 7-10 are generated by running a nested loop. For each given RWA isolator cutoff frequency, optical control bandwidth is varied over its full range. This gives us a full array of performance values for every RWA isolator cutoff frequency/optical control bandwidth combination.

Figure 7-9 shows OPD13 isoperformance contours. By isoperformance we mean that there exists a range of design parameter combinations that will result in the same performance output. Any point on a curve marked with the same number will result in the same OPD13 RMS output. The OPD performance requirement of 1.01 nm is

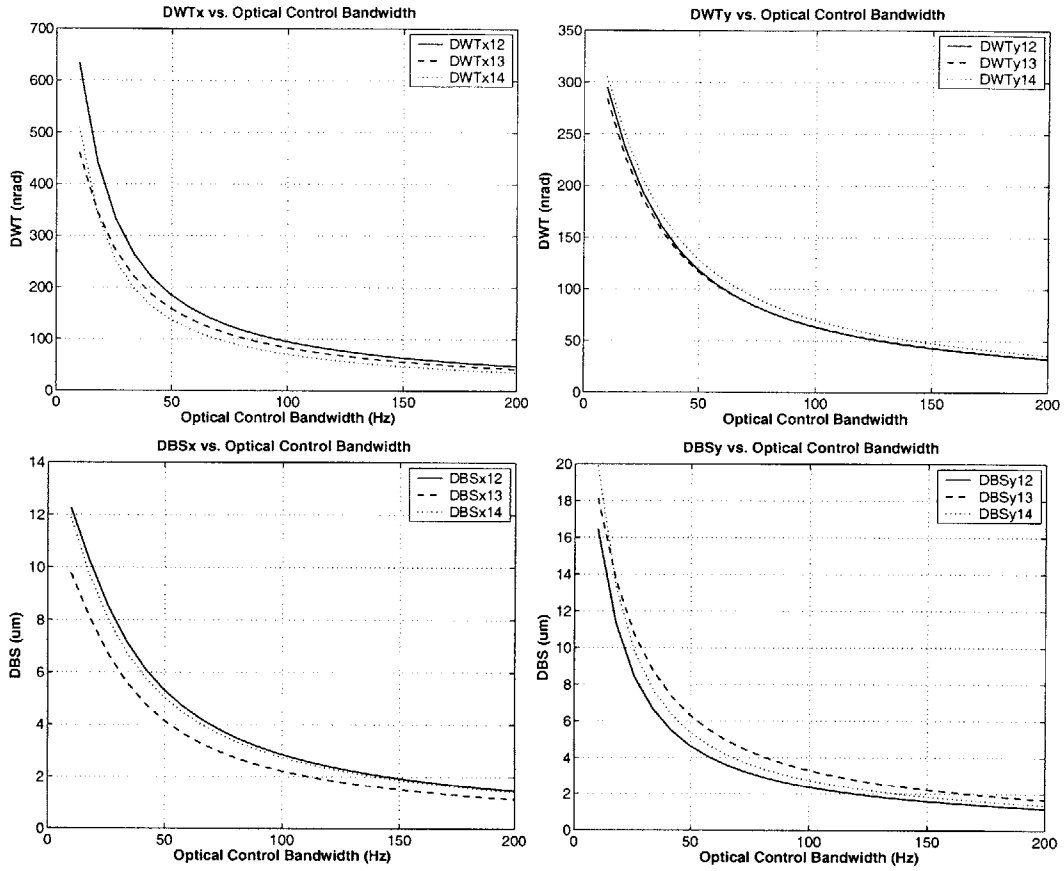

Figure 7-8: DWT and DBS as a function of Optical Control Bandwidth

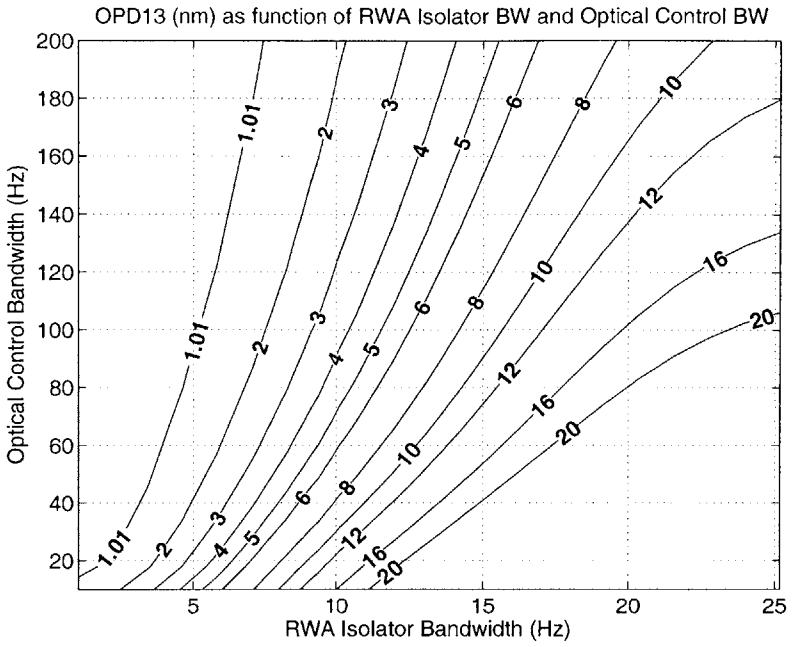

Figure 7-9: Isoperformance contours for OPD13 as a function of RWA isolator cutoff frequency and optical control bandwidth.

labelled as its own curve. Any point on or above this line will define a combination of optical control bandwidth and RWA isolator cutoff frequency that will fall within the OPD requirement. We can also see from this curve that in general we want to decrease RWA isolator cutoff frequency and increase optical control bandwidth to improve performance. This trend is found across all of the performance metrics. Figure 7-10 shows contour plots for DWT12 and DBS12 for both x and y. Each of these plots has a curve with the nominal performance requirement labelled as well.

7.2.2 "DesignVector" Variations: Truss Geometry

One area of possible design variability is in the truss geometry. The number and size of the bays are elements of `DesignVector` that may be changed before creating the integrated model. A structurally connected interferometer for TPF will likely have a hinge in the middle of the truss so that the spacecraft can be folded up when it is stowed in the fairing of a launch vehicle. Figure 7-11 shows an artist's rendition of

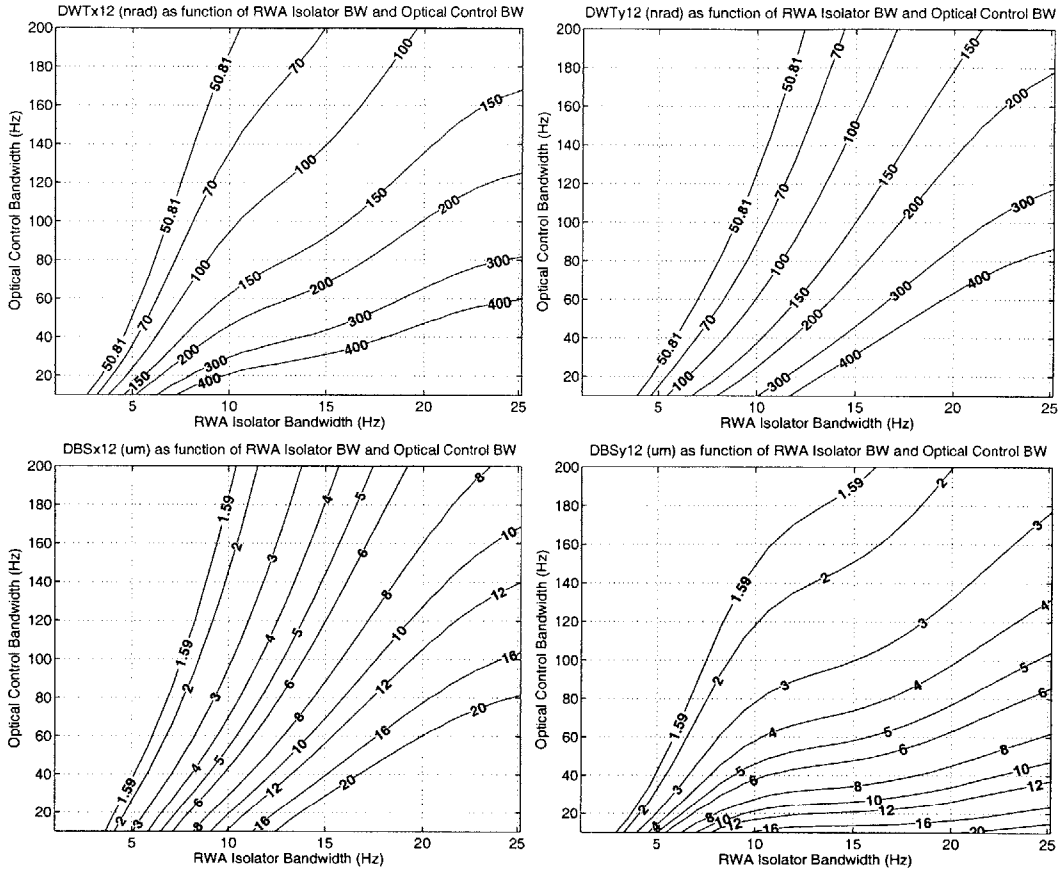

Figure 7-10: Isoperformance contours for DWT12 and DBS12 as a function of RWA isolator cutoff frequency and optical control bandwidth

the stowed TPF in the fairing of a Delta IV Heavy launch vehicle [14]. Because of the limited choices in launch vehicles, size will be a constraint on the structural design.

Our nominal truss design calls for one meter cubic bays along the entire baseline. One hypothesis is that it may be possible to improve performance by using a symmetrically tapered truss. This is based upon the fact that the internal bending moment of a cantilevered beam is at its maximum at the base and falls off linearly to zero at the tip. Similarly, the ends of the truss do not need to provide a significant bending moment to keep the spacecraft stiff. Moreover, a tapered truss might fit more easily into a launch vehicle fairing.

One of the inputs to the MATLAB code that generates the FEM is an array of truss bay heights and widths. This array defines the locations of all the grid points in the truss so it is possible to generate a linearly tapered truss with one end of a bay smaller than its other end. Figure 7-12 shows an example of a linearly tapered truss with an end height of 0.2 m and an end width of 0.6 m. The cross-sectional dimensions of each bay in the truss can be varied so that it is possible to create non-linear shapes in the truss as well.

One interesting trade is to determine the effect of truss taper on first mode frequency while keeping overall mass constant. For this trade, the bays are constrained to have square cross-sections and symmetric, linear tapers. The mass is held constant by increasing the dimensions of the center bay by the same amount that the outer bays are decreased.

Figure 7-13 shows the results of ten variations in truss taper. First mode frequency is given as a function of taper percentage. Taper percentage refers to the percentage decrease in the cross-sectional dimension of the end bay. For a run where the middle bay is changed to a 1.3m$\times$1.3m square cross-section and the end bay is a 0.7m$\times$0.7m cross-section, the taper percentage will be 30%. The plot shows that first mode frequency increases with taper percentage until taper percentage is about 50%. After this point the first mode frequency falls off quickly.

As first mode frequency increases, intuition tells us that the optical performance should also improve. Currently, the trends in optical performance are inconclusive.

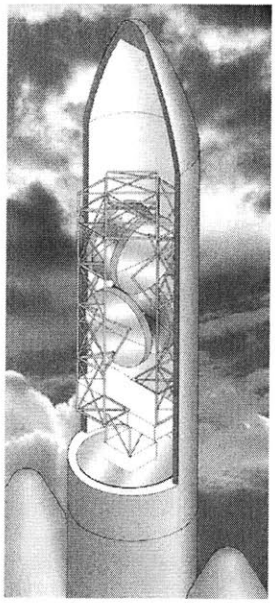

Figure 7-11: Stowed TPF in Delta IV Heavy launch vehicle [14]

Possible reasons for this will be explained in the future work section of Chapter 8.

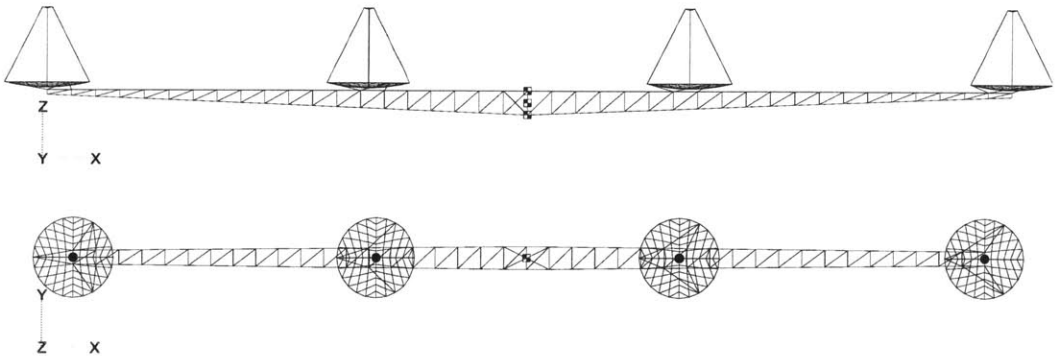

Figure 7-12: Tapered truss with end height=0.2 m, end width=0.6 m.

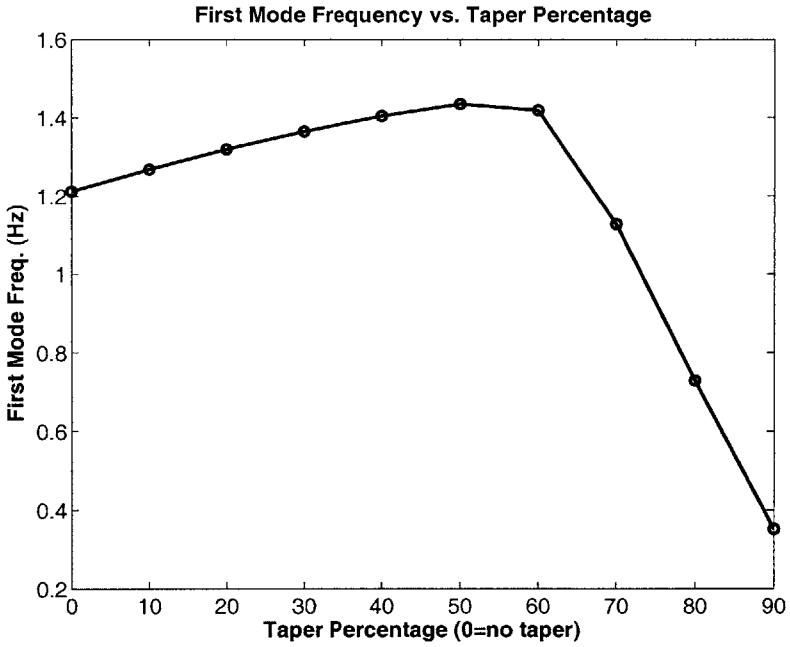

Figure 7-13: First flexible mode frequency vs. taper percentage. Truss bays are given square cross-sections. The taper percentage corresponds to the linear dimension of the edge of the last bay.

Chapter 8

Conclusions and Recommendations

In this thesis we have created an integrated model of the Structurally Connected Interferometer for TPF that can predict optical performance and be used in design trades. By creating the model in a modular state-space form using the DOCS environment, it is very upgradeable and expandable. Higher fidelity subsystem models can replace current models and new components can be added to the integrated model as the design process moves forward. Additionally, the integrated model generation is automated through the use of MATLAB allowing for easy regeneration with changes in a wide variety of design parameters.

A CODE-V/MATLAB toolbox has been created to automate the sensitivity calculations for optical systems. This will be useful not only for changes in the TPF optical design but for a wide variety of future optics applications.

Since the TPF integrated model is designed to be continually refined and broadened in scope, it is fitting to now offer suggestions as to how work may continue with this model.

8.1 Expand and Upgrade Integrated Model

Benefiting from the integrated model upgradeability and expandability, future work can be done in the areas of thermal modeling, disturbance modeling, and FEM refinement.

8.1.1 Thermal Modeling

During operations, TPF will undergo variations in heat exposure and its structure will expand and contract as a result. This will alter the position of the mirrors and have an effect on optical performance. The thermal source and expansion properties of the structure must be modeled. In addition, the damping ratio of the truss material may significantly decrease at cryogenic temperatures. It will likely be found that aluminum will not meet the thermal requirements for TPF. Design trades should be performed to determine what materials will meet the requirements.

8.1.2 Disturbances

Since optical performance is dependent on spacecraft disturbances, work should continue in refining current disturbance models and adding models of new disturbance sources. The current RWA disturbance models are based upon load cell data of a reaction wheel hard mounted to a table in a laboratory. In the space environment, coupling will occur between the reaction wheel and the spacecraft causing changes in the disturbance spectrum. The effect of these changes should be quantified and added into the model if necessary.

As explained in Chapter 5, the sensor noise model is still somewhat crude due to the lack of knowledge about the TPF optical sensor characteristics. Since null stability is dependent on this sensor noise, and will likely be a driving factor in the optical performance requirements, work should continue in determining the properties of these sensors so that more accurate models can be made.

There are a variety of other disturbance sources that may also need to be modeled. Devices will be needed to cool the optical sensors on TPF. These devices will operate at a given drive frequency and will cause a harmonic disturbance [8]. Optical delay line servomechanisms and tip-tilt mirrors will cause reaction forces on the spacecraft when they are actuated. Similar to reaction wheels, rate gyros will have imbalances in their spinning elements that will cause harmonic disturbances. These are just a few of the additional disturbances that can be modeled for TPF.

8.1.3 FEM Refinement

The FEM can be refined in a number of ways. First, it is expected that the truss will be folded before it is stowed in a launch vehicle fairing. It will be useful to model the hinge in the center of the truss so that its effect on performance is understood. Also, there are other flexible appendages on a spacecraft that can be added to this model. This includes solar arrays, antennas and sun-shields. Detail should be given to the combiner and bus that are currently modeled as point masses. An improved optical model will be possible if the combiner is accurately modeled in the FEM.

8.2 Design Trades

Additional design trades should also be performed so that more methods of improving performance can be devised. In particular, structural design parameters such as stiffness, area and density should be made DOCS perturbable parameters. Some work has already begun in this areas but the results are currently inconclusive. In Chapter 7 we noted that even though first mode frequency increases with truss taper, the optical performance does not follow the same expected trend. Similar results are found when varying truss stiffness.

8.2.1 Truss Stiffness

This section explains an effort that has begun to create a new DOCS perturbable parameter for truss modulus. A set of DOCS functions are used to find sensitivities to FEM parameters. Using these sensitivities, changes in performance outputs due to changes in these inputs can be calculated very quickly without the need to rerun the FEM code. Figure 8-1 show the results of a DOCS perturbation analysis for truss modulus. This analysis includes 1000 points between modulus values of 0.8-1.2 times the nominal value. The graph looks very sinusoidal and seems to show that optical performance is extremely sensitive to truss modulus over small ranges. The global trend may even suggest that optical performance worsens as the truss stiffens, counter

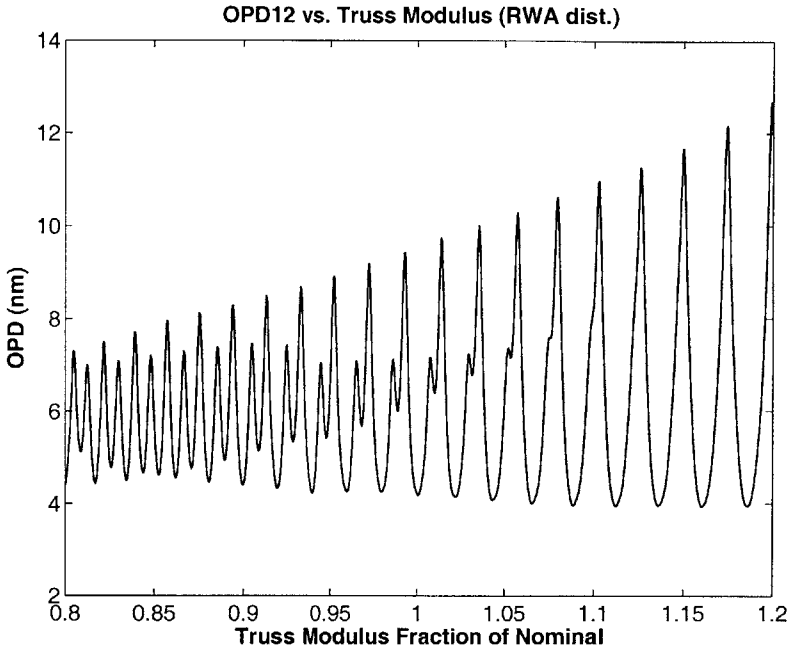

Figure 8-1: Truss stiffness perturbations with RWA broadband disturbance

to intuition.

One concern was that the RWA broadband disturbance might be causing the extreme sensitivities in the curve. The RWA PSD disturbance has a saw-tooth shape at the higher frequencies that might cause the swings in OPD as the mode shapes move and get excited by the teeth of the disturbance PSD. To investigate this, the disturbance source was replaced by white noise. Figure 8-2 shows the result of this analysis. This curve also exhibits sinusoidal patterns and has a large spike just above the nominal truss value. This indicates that the shape of the RWA PSD is likely not the cause of the OPD oscillations in truss stiffness sensitivity.

This is an area where more work is required to either validate the results of Figure 8-1 or determine the cause of the error. Once this is solved, more trades can be performed by varying the material properties of the mirrors and the mirror supports.

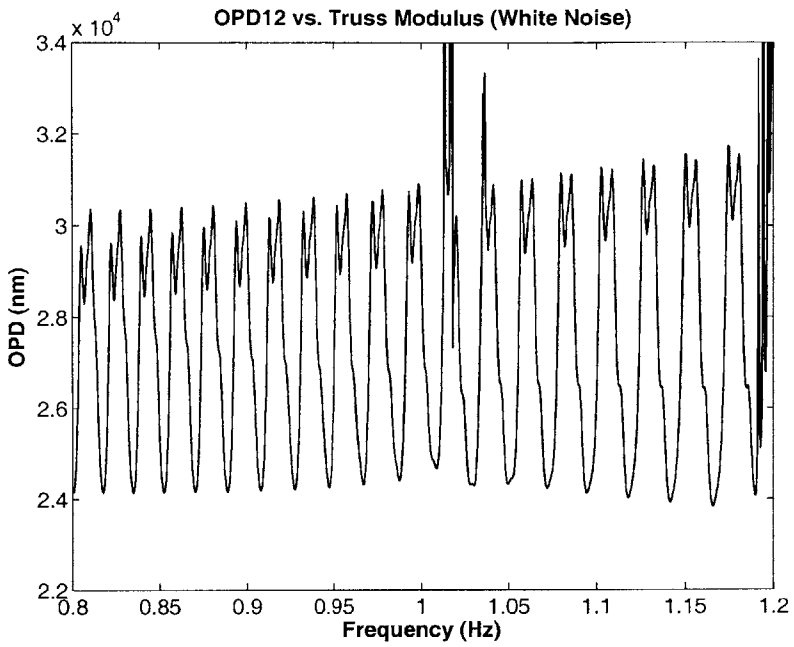

Figure 8-2: Truss stiffness perturbations with white noise disturbance

8.3 Related Research

Finally, because of its automation and adaptability, the integrated model of TPF will be a useful tool in a wide variety of research areas. Those with an interest in an individual area such as structural dynamics or control theory will be able work within that particular subsystem without having to worry about adjusting the models of the rest of the spacecraft. Since many of the TPF components are non-unique, this integrated model can also serve as a template for future space systems models.

Two specific research areas in which this model will likely be used are "uncertainty analysis" and "tailoring and tuning."

8.3.1 Uncertainty Analysis

Oftentimes it is very difficult to predict the exact properties of materials or the exact behavior of disturbances. There are uncertainties associated with values that will propagate through the construction of a spacecraft and may result in vastly different

performance than that which is predicted. This is the motivation behind uncertainty modeling and analysis. The idea is to model these uncertainties early in the design process and keep track of how they would propagate in a fully assembled spacecraft. Uncertainty bounds can then be created in which a range of performance can be guaranteed. Utilizing the DOCS environment, perturbable parameters can be created through which uncertainties can be propagated in the TPF model.

8.3.2 Tailoring and Tuning

"Tailoring and tuning" is another area of research related to the problem of uncertainty in performance predictions. The idea here is to determine if methodologies can be created by which a spacecraft can be tuned to improve its performance once construction is complete [24]. Possible methods include adding masses in certain areas to change mode shapes and reduce optical jitter. This can be taken further to actually "tailor" a spacecraft for tuning so that it is specifically designed for adjustments to be made in terms of mass or geometry after construction is complete. This TPF model can be used to analyze what types of tailoring and tuning methods will work best.

Bibliography

[1] *ZEMAX Optical Design Program User's Guide Version 9.0.* Focus Software, Incorporated, 2000.

[2] Alan Dressler, et. al. *Origins: Roadmap for the Office of Space Science Origins Theme.* Jet Propulsion Laboratory, 2003.

[3] Robert Brown and Patrick Hwang. *Introduction to Random Signals and Applied Kalman Filtering.* John Wiley & Sons, 1997.

[4] C. Noecker, O. Lay, B. Ware, and S. Dubovitsky. TPF interferometer performance requirements. *Proceedings of SPIE Vol. 5170 Techniques and Instrumentation for Detection of Exoplanets*, 2003.

[5] Soon-Jo Chung. LOS Sensitivities for FOCAL and AFOCAL telescopes Ver 2.0. MIT Space Systems Lab Research Memo, December 19, 2003.

[6] Newport Corp. http://www.newport.com/file_store/Optics_and_Mechanics/ Optical_Systems/FSM/FSM/PDF_Files/FSM_Application_Note2.pdf.

[7] David C. Redding and William G. Breckenridge. Optical Modeling for Dynamics and Control Analysis. *AIAA Guidance, Navigation, and Control Conference*, 1990.

[8] Olivier de Weck. *Integrated Modeling and Dynamics Simulation for the Next Generation Space Telescope.* Master's thesis, Massachusetts Institute of Technology, 1999.

[9] George Angeli, et. al. Integrated Modeling Tools for Large Ground Based Optical Telescopes. 2003.

[10] Robert L. Grogran and Robert A. Laskin. On Multidisciplinary Modeling of the Space Interferometry Mission. *Proceedings of the American Conctrol Conference*, pages 1558–1562, June 199.

[11] The TPF Science Working Group. *Terrestrial Planet Finder (TPF): A NASA Origins Program to Search for Habitable Planets.* Jet Propulstion Laboratory, 1999.

[12] Homero Gutierrez. *Performance Assesment and Enhancement of Precision Controlled Structures During Conceptual Design.* PhD thesis, Massachusetts Institute of Technology, February 1999.

[13] Thomas I. Harris. *CODE V Prompting Guide.* Optical Research Associates, 2003.

[14] Curt Henry. TPF Interferometer Design Team. Presentation at the January 14, 2004 Science Working Group meeting.

[15] Joseph M. Howard. Optical Modeling Activities for the James Webb Space Telescope (JWST) Project: 1. The Linear Optical Model. *Optical Modeling and Performance Predictions, Proceedings of SPIE*, 5178:82–88, 2004.

[16] http://mathworld.wolfram.com/ConicSection.html.

[17] http://planetquest.jpl.nasa.gov/.

[18] http://www.du.edu/ jcalvert/math/ellipse.htm.

[19] http://www.jwst.nasa.gov/.

[20] http://www.photonics.com/dictionary/.

[21] Mike Lieber. Development of the Ball Integrated Telescope Model (ITM). *SPIE: Integrated Modeling of Telescopes*, 4757:19–30, 2002.

[22] Kuo-Chia Liu. *Stochastic Performance Analysis and Staged Control System Designs for Space Based Interferometers.* PhD thesis, Massachusetts Institute of Technology, May 2003.

[23] Rebecca A. Masterson. *Development and Validation of Empirical and Analytical Reaction Wheel Disturbance Models.* Master's thesis, Massachusetts Institute of Technology, June 1999.

[24] Rebecca A. Masterson and David W. Miller. Dynamic Tailoring and Tuning for Precision Optical Space Structures. *45th AIAA/ASME/ASCE/AHS/ASC Structures, Structural Dynamics & Materials Conference*, 2004.

[25] Leonard Meirovitch. *Elements of Vibration Analysis.* McGraw Hill, 1986.

[26] James W. Melody. Discrete-Frequency and Broadband Reaction Wheel Disturbance Models. JPL Interoffice Memorandum. June 1, 1995.

[27] Michael Muller, et. al. Integrated Modeling for the VLTI. *Interferometry for Optical Astronomy II, Proceedigns of SPIE*, 2003.

[28] Gregory W. Neat, James W. Melody, and Boris J. Lurie. Vibration Attenuation Approach for Spaceborne Optical Interferometers. *IEEE Transactions on Control Systems Technology*, 6(6):689–700, November 1998.

[29] C. Perrygo and R. Burg. Hand calculation of line-of-sight sensitivity to optics displacements. NGST Systems Engineering Memo, January 22,1999.

[30] Douglas G. Thayler. *Multi-Sensor Control for 6-Axis Active Vibration Isolation.* PhD thesis, University of Washington, 1998.

[31] Paul Wirsching, Thomas Paez, and Keith Ortiz. *Random Vibrations.* John Wiley & Sons, 1995.